

RICE UNIVERSITY

**Observation of antiferromagnetic correlations in the Fermi-Hubbard
model**

by

Pedro M Duarte

A THESIS SUBMITTED
IN PARTIAL FULFILLMENT OF THE
REQUIREMENTS FOR THE DEGREE

Doctor of Philosophy

APPROVED, THESIS COMMITTEE:

Randall G. Hulet, *Chair*
Fayez Sarofim Professor of Physics and
Astronomy

Thomas. C. Killian
Professor of Physics and Astronomy

Peter Wolynes
Bullard-Welch Foundation Professor of Science
Professor of Chemistry and
Materials Science & NanoEngineering
Professor of Physics and Astronomy

HOUSTON, TEXAS

OCTOBER 2014

ABSTRACT

Observation of antiferromagnetic correlations in the Fermi-Hubbard model

by

Pedro M Duarte

The Hubbard model contains only the essential ingredients to describe the behavior of strongly interacting electrons moving in a periodic lattice. It describes particles that can tunnel between sites in the lattice and that acquire an on-site interaction energy when two of them occupy the same lattice site. This simple model is a prominent example of how strongly correlated phases emerge from simple Hamiltonians. It gives rise to a Mott-metal insulator transition, and at a density of one particle per site shows an antiferromagnetic ground state. It is also considered to contain the essence of high-temperature superconductivity as observed in the cuprates, a question that remains open due to the difficulty in numerically accessing the solutions of the model at densities different from one particle per site.

In this work we have realized the Hubbard model with a spin mixture of ultracold atoms in a simple cubic optical lattice. Atoms in lattices have emerged in the last decade as promising systems in which to perform quantum simulations of condensed matter Hamiltonians. In the laboratory we can create defect-free optical lattice potentials with laser light, and we can control the interactions between the atoms using a magnetic Feshbach resonance.

For this work we implemented a novel compensated optical lattice setup, which allows us to control the density of the sample and mitigate the non-adiabaticity in the lattice loading process which often leads to heating of the sample or to out of equilibrium distributions. Using the compensated optical lattice we are able to get closer to the ground state of the Hubbard model than anybody before us has been able to do with ultracold atoms.

To demonstrate this achievement we use spin-sensitive Bragg scattering of light to mea-

sure the spin-structure factor, a measure of the antiferromagnetic correlations in the collection of spins. Measurements of the spin-structure factor are compared to results of theoretical calculations to establish precise thermometry for the atoms in the lattice. We have also studied the *in-situ* density distribution of the system, which confirms that the temperature of our sample is in a regime where most of the remaining entropy in the system resides in the spin degrees of freedom.

The results presented here represent an important step in the field of quantum simulation using ultracold atoms. In the future, we expect to further explore and exploit the experimental possibilities opened up by the compensated lattice potential and by light scattering thermometry, with the ultimate goal of addressing the existence of *d*-wave superfluidity in the Hubbard model.

Table of Contents

1 Many body physics with ultracold atoms	1
1.1 Motivation: Strongly correlated materials	1
1.2 Quantum simulations with ultracold atoms	4
1.3 Quantum magnetism with ultracold atoms	6
1.4 This thesis	9
1.4.1 Outline	10
2 Ultracold atoms in optical lattices	11
2.1 One-dimensional optical lattice potential	11
2.1.1 Band structure	13
2.1.2 Eigenstates	14
2.1.3 Wannier states	15
2.2 Three-dimensional optical lattice potential	16
2.3 Hubbard Hamiltonian	18
2.3.1 Second quantization	19
2.3.2 Operators in second quantization	21
2.3.3 Second quantized Hubbard Hamiltonian	24
2.4 Parameter regimes for a valid description using a single band Hubbard model	31
3 The Hubbard model	33
3.1 A bit of history	33
3.2 Hubbard model for a single lattice site, $t = 0$	35

Chapter	Page
3.3 Particle-hole symmetry	38
3.4 Exact diagonalization	38
3.5 High-temperature series expansion	46
3.6 Local density approximation	50
3.7 Latest developments in numerical techniques	51
4 Overview of the experimental setup	55
4.1 Vacuum system	57
4.2 671 nm laser cooling system	58
4.2.1 Laser system	58
4.2.2 Zeeman slower	60
4.2.3 2DMOT and MOT	60
4.3 323 nm laser cooling system	63
4.3.1 Laser system	63
4.3.2 UVMOT	64
4.3.3 Transfer from MOT to UVMOT	66
4.4 Optical dipole trap	67
4.5 Magnetic field	70
4.6 Loading the ODT	71
4.7 Compensated optical lattice	76
4.7.1 Optical lattice and dimple	76
4.7.2 Compensation	77
4.8 Diagnostics	78
4.9 Control, automation, and data analysis	80
5 Compensated optical lattice potential	83

Chapter	Page
5.1 Form of the potential	86
5.2 General aspects	87
5.3 Local density approximation	94
5.3.1 Format for presentation of LDA results	95
5.3.2 Entropy redistribution	100
5.4 Results	102
5.4.1 Atom number	104
5.4.2 Timescales for locking the lattice	105
5.5 Comparison between different kinds of traps	107
6 Diagnostic tools I: Polarization phase-contrast imaging	111
6.1 Polarization phase-contrast imaging	112
6.1.1 Transmission of light through a polarized gas	114
6.1.2 Polarization of the cloud	116
6.1.3 Susceptibility for ${}^6\text{Li}$ atoms at high magnetic field	119
6.1.4 Change in field parameters due to atomic column density	123
6.1.5 Experimental setup for PPCI	124
6.1.6 Results	127
7 Diagnostic tools II: Fermi gas thermometry	129
7.0.7 Density distributions of a trapped Fermi gas	130
7.0.8 Time-of-flight	132
7.0.9 Column density and imaging geometry	133
7.0.10 Fitting functions	135
8 Diagnostic tools III: Double occupancy	137
8.1 ${}^6\text{Li}$ Feshbach resonances	138
8.2 Measurement procedure	140

Chapter	Page
8.3 Measurements in a compensated lattice	142
8.4 <i>In-situ</i> measurement of double occupancies	143
8.5 Measurement systematics	143
9 Diagnostic tools IV: Bragg scattering of light	147
9.1 Coherent light scattering by an array of atoms.	149
9.1.1 Non-interfering term and incoherent scattering	153
9.1.2 Coherent scattering	154
9.1.3 Crystal structure	155
9.1.4 Magnetic structure	155
9.1.5 Time-of-flight	157
9.2 Experimental setup	158
9.2.1 Diffuse background	160
9.3 Measurement of the crystal structure factor	161
9.3.1 Angular dependence of the scattering	162
10 Experimental procedures	167
10.1 Production of a deeply degenerate ${}^6\text{Li}$ spin mixture in a dimple potential	168
10.1.1 Optimized trajectory for evaporation in the ODT	168
10.1.2 Modifications to the trajectory for evaporating into the dimple	173
10.2 Lattice alignment procedure	174
10.3 Lattice loading ramps	178
11 Mott insulating state in a simple cubic lattice	181
11.1 Summary	187
12 Antiferromagnetic correlations in the Hubbard model	189

Chapter	Page
12.1 Technical details	189
12.1.1 Momentum transferred from the probe to the atoms.	191
12.1.2 Optical density.	192
12.1.3 Light collection.	193
12.1.4 Data averaging.	193
12.2 Time-of-flight	194
12.3 Numerical calculations	195
12.4 Bragg signal optimization	196
12.5 Spin structure factor	197
12.5.1 Atom number	200
12.5.2 Decay of Bragg signal with hold time in the lattice	201
12.5.3 Entropy	201
12.6 Summary	203
13 Conclusion	205
A Compensated optical lattice potential	207
A.1 Dipole potential and scattering rate	207
A.2 Compensated lattice potential: definitions and simplified expressions	208
A.2.1 Electric field	209
A.2.2 Lattice depth	210
A.2.3 Lattice and dimple radial frequencies	211
A.2.4 Compensation beams	212
A.3 Fermi temperature for a compensated dimple	213
A.4 Heating	214
A.5 Heating due to optical lattice beams	216

Chapter	Page
A.6 Heating due to green compensation beams	218
A.7 Total heating rate in the compensated lattice	218
A.8 Total heating rate in the compensated lattice	219
B Numerical calculations for the Hubbard Hamiltonian in the compensated lattice	221
B.0.1 NLCE	221
B.1 Complete NLCE data set	222
B.2 Spin structure factor	222
B.2.1 Effective fraction	225
B.3 NLCE data	226
B.4 QMC data	228
B.5 NLCE data and QMC data comparison	228
B.6 Comparison of experimental data with LDA	228
B.6.1 Determination of Spi/n by interpolation	230
B.6.2 LDA density profiles with NLCE data, dependence on T	231
B.6.3 LDA S_π/n profiles, lowest accessible T variation of N	232
B.6.4 \bar{S}_π vs. N for various T 's	235
BIBLIOGRAPHY	237

12. Antiferromagnetic correlations in the Hubbard model

The contents of this chapter are based on a paper that has been submitted for publication, titled “Observation of antiferromagnetic correlations in the Hubbard model with ultracold atoms” [143].

For this experiment we realize the Hubbard model in a $7 E_r$ lattice with repulsive interactions. We vary the interaction strength U_0/t_0 in the range $3.1 < U_0/t_0 < 21.4$. For each value of the interaction strength we measure the spin structure factor of the system S_Q as a function of atom number (in the range of 1 to 2.5×10^5 atoms). We find that, for a momentum transfer $\mathbf{Q} = \pi \equiv \frac{2\pi}{a}(-\frac{1}{2}, -\frac{1}{2}, +\frac{1}{2})$, which satisfies the Bragg condition for scattering from a magnetically ordered sample, S_π ~~is sharply peaked with respect to atom number~~ ^{~~shows a maximum~~} ^{*couple them results to*}. We plot the maximal S_π at each value of U_0/t_0 vs. U_0/t_0 , and also plot results of numerical calculations at different temperatures. From the comparison ~~between the data and the results of calculations~~, we can quantitatively extract the temperature of the system in a previously unexplored regime, where the entropy is mostly contained in the spin degree of freedom.

12.1 Technical details

A schematic of the setup for Bragg scattering is shown in Fig. 12.1. As was mentioned in Chapter 9, we obtain spin sensitivity, ~~in analogy to neutron scattering used to characterize magnetism in solid state materials~~, by setting the Bragg laser frequency between the optical transition frequencies for states $|1\rangle$ and $|2\rangle$. The spin structure factor, S_Q , defined in Eq. 9.28 is obtained by measuring the ratio of *in-situ* and TOF intensities scattered with momentum transfer \mathbf{Q} . Measurements of the scattered intensities are taken after locking the lattice to

time-of-flight (TOF)

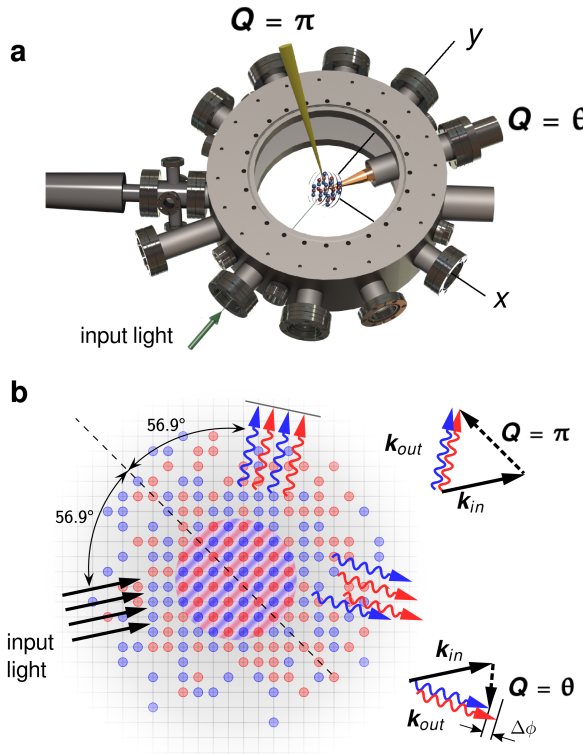


Figure 12.1: Schematic depiction of Bragg scattering. **a**, Rendering of the experimental setup used for Bragg scattering. Light is collected for momentum transfers $\mathbf{Q} = \pi$ and $\mathbf{Q} = \theta$. The x and y axes of the coordinate system (right handed) are shown. A bias magnetic field, which sets the quantisation axis and the interaction strength, points in the z direction. The input Bragg beam lies in the yz plane, and its wavevector makes an angle of 3° with the positive y axis. **b**, The two spin states are denoted by red and blue circles. AFM order develops at the Mott plateau, shown here to be located in the centre, where $n \simeq 1$. AFM correlations are suppressed outside the central region where $n < 1$. Bragg scattering requires the input and output wavevectors, \mathbf{k}_{in} and \mathbf{k}_{out} , respectively, to satisfy the Bragg condition $\mathbf{k}_{out} - \mathbf{k}_{in} = \pi$. The red and blue arrows denote light scattered from one spin state or the other. The two spin states scatter with opposite phase shift, so that their respective sublattices interfere constructively. For a different momentum transfer $\mathbf{k}_{out} - \mathbf{k}_{in} = \theta$, scattering is relatively insensitive to AFM correlations due to the lack of constructive interference between the scattered photons, which have random relative phases $\Delta\phi$.

a depth of $20 E_r$.

$$\mathbf{Q}$$

We measure the spin structure factor for two values of the momentum transferred which are labeled π and θ . The Bragg condition is satisfied for $\mathbf{Q} = \pi$ but not for $\mathbf{Q} = \theta$, so the results at θ serve as a control for the experiment. Figure 12.1 illustrates the two different

values of the momentum transfer ~~with respect to the vacuum chamber~~. The components of the momentum transfer vectors corresponding to π and θ are

$$\begin{aligned}\pi &= \frac{2\pi}{a}(-0.5, -0.5, +0.5) \\ \theta &= \frac{2\pi}{a}(+0.396, -0.105, -0.041).\end{aligned}$$

As was mentioned in Chapter 9, it is important to include the effects of saturation of the atomic transition when obtaining the spin structure factor from the measured intensities. Here, the Bragg probe beam is a collimated Gaussian beam, with a $1/e^2$ radius of $450\ \mu\text{m}$ and power of $250\ \mu\text{W}$. The saturation parameter is $s_0 = 15.5$ and the detuning is $|\Delta| = 6.4$, which results in a correction due to saturation effects

$$1 + \frac{s_0}{4\Delta^2} = 1.09. \quad \text{(in units of } \textcircled{P}) \quad (12.1)$$

In addition, one must include the Debye-Waller correction due to the finite extent of the atomic wavefunctions in the $20 E_r$ lattice. We have respectively

$$e^{2W_\pi(\tau=0)} = 1.52$$

$$e^{2W_\theta(\tau=0)} = 1.18$$

Besides the saturation of the transition and the Debye-Waller factor, which were discussed in Chapter 9, there are additional considerations ~~that must be taken into account~~ for this measurement. We comment on them in the sections below.

12.1.1 Momentum transferred from the probe to the atoms.

In the derivation of the relationship between the intensity and the structure factor, showed in Chapter 9, we assumed that the center of mass state of the atom remains unchanged after scattering a photon. For this assumption to be valid, the Lamb-Dicke parameter, η^2 , which relates the energy of the photon to the harmonic oscillator spacing in

a lattice site¹, needs to be $\eta^2 \ll 1$. In the locked $20 E_r$ lattice, $\eta^2 = 0.27$, meaning that approximately one out of every 4 photons scattered will excite an atom to the second band of the lattice. An atom in the second band has larger position variance and therefore a smaller Debye-Waller factor, so it contributes less to the Bragg scattering signal.

by each atom

The total number of photons scattered is given by $t_{\text{exp}} \Gamma \frac{s_0/2}{s_0 + 4\Delta^2}$, where the duration of the probe is $t_{\text{exp}} = 1.7 \mu\text{s}$ and the linewidth of the excited state is $\Gamma = 1/27 \text{ ns}^{-1}$. For $s_0 = 15.5$ and $\Delta = 6.4$ ns^{-1} this corresponds to 2.7 photons scattered per atom during the probe pulse. In a $20 E_r$ lattice it is then justifiable to assume the atoms remain in the lowest band during the pulse.

Nevertheless,

For the Bragg scattering measurements performed after time-of-flight, the momentum transferred from the probe to the atoms plays a more significant role, since the atoms are not trapped and will recoil after every photon scatter. ~~As we will show in the measurements below (Fig. 12.2),~~ we still see good agreement between the observed decay of the Bragg scattering signal in time-of-flight and the decay expected for a Heisenberg limited wavepacket (Eq. 9.33). A similar consideration arises for Bragg scattering off of the $(0 1 0)$ lattice planes, where in Chapter 9 we saw that there was good agreement with Eq. 9.33.

12.1.2 Optical density.

A low optical density of the sample is important so that the probe is unattenuated through the atom cloud, and multiple scattering events of the Bragg scattered photons are limited[58]. The optical density can be approximated as

$$\text{OD} \simeq \frac{\sigma_0 |\hat{e}_p \cdot \hat{e}_{-1}|^2}{4\Delta^2 + s_0} \frac{1}{a^2} \left(\frac{3N}{4\pi} \right)^{1/3}$$

where $\sigma_0 = 3\lambda_0^2/2\pi$. With $s_0 = 15.5$, $\Delta = 6.4 \text{ ns}^{-1}$ and $N = 1.8 \times 10^5$ atoms we have $\text{OD} \simeq 0.072$. At this value we do not expect significant corrections to the spin structure

¹

$$\eta^2 = \hbar\omega_{\text{in}}/(2E_r \sqrt{v_0/E_r}) \quad (12.2)$$

where ω_{in} is the angular frequency of the incident light, and v_0 is the lattice depth.

factor measurement due to the attenuation of the probe. We do not include any corrections in our measurement due to finite optical density effects.

12.1.3 Light collection.

We collect Bragg scattered light in the π direction over a full angular width of 110 mrad, given by a 2.5 cm diameter collection lens located 23 cm away from the atoms. In the θ direction, light is collected by a 2.5 cm diameter lens placed 8 cm away from the atoms, corresponding to a full angular width of 318 mrad. The scattered light in each of the directions is focused to a few pixels on the cameras, so no additional angular information is obtained. For $N = 1.8 \times 10^5$, $s_0 = 15.5$, $\Delta = 6.0\text{mT}$ and a $1.7\mu\text{s}$ pulse, the detector in the π direction collects approximately 1300 photons, whereas the detector in the θ direction collects approximately 10^4 photons. The noise floor from readout, dark current and background light per shot has a variance equivalent to approximately 250 photons in the π direction and 1000 photons in the θ direction.

12.1.4 Data averaging.

The signals we detect are small enough that an uncorrelated sample may, in a single shot, produce a scattering signal as large as the ones produced by samples with AFM correlations. To obtain a reliable measurement of S_π we average at least 40 *in-situ* shots to obtain I_{Q0} and at least 40 time-of-flight shots to obtain $I_{Q\infty}$.

We estimate the expected variance on S_π by considering a randomly ordered sample in which $e^{i\boldsymbol{\pi} \cdot \mathbf{R}_n} 2\langle \sigma_z \rangle_n$ is equal to +1 or -1 with equal probability. S_π can be written as

$$S_\pi = \left| \sum_n e^{i\boldsymbol{\pi} \cdot \mathbf{R}_n} \frac{2\langle \sigma_z \rangle_n}{\sqrt{N}} \right|^2,$$

which is equivalent to the square of the distance travelled on an unbiased random walk with step size $1/\sqrt{N}$. The mean and standard deviation can then be readily calculated: $\overline{S_\pi} = 1$ and $\sqrt{\text{Var}(S_\pi)} = \sqrt{2}$, where $\text{Var}(S_\pi)$ denotes the variance of the random variable

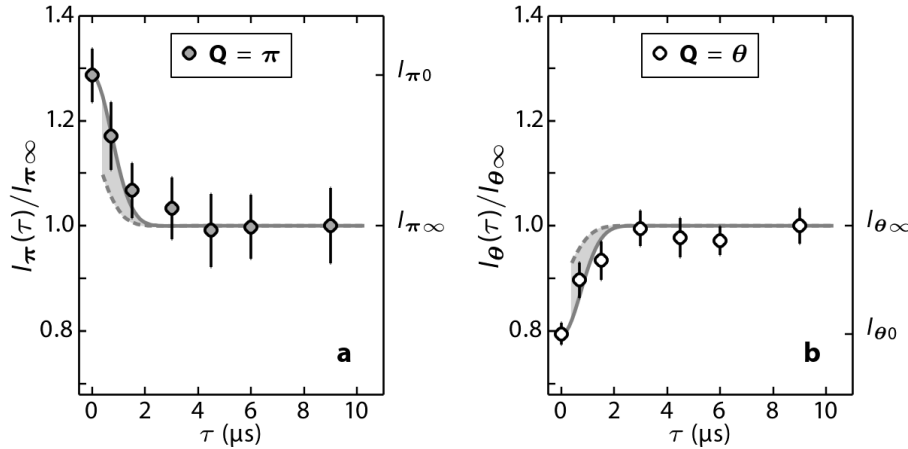


Figure 12.2: Time-of-flight measurement of scattered intensity from a sample with AFM correlations. **a**, Normalised intensity of Bragg scattered light ($Q = \pi$) as a function of time-of-flight τ . The *in-situ* ($\tau = 0$) scattered intensity is denoted as I_{Q0} , while the intensity after sufficiently long τ , corresponding to an effectively uncorrelated sample, is denoted as $I_{Q\infty}$. **b**, For $Q = \theta$ the *in-situ* sample shows a reduction of scattering as compared to long τ . Each data point and error bar is the mean and standard error (SE) of at least 17 measurements of the scattered intensity. The grey solid line is the intensity calculated using the value of the Debye-Waller factor at τ , whereas the dashed grey line uses the average value of the Debye-Waller factor during the 1.7 μs exposure of the Bragg probe.

S_π . With a standard deviation that is larger than the mean value, a considerable number of shots needs to be taken in order to obtain an acceptable error in the mean. The standard error of the mean for 40 shots will be $\sqrt{2/40} = 0.22$, consistent with what we obtain in the experiment (cf. vertical error bars in Fig. 12.6).

★ MOVE TECHNICAL DETAILS TO THE END .

12.2 Time-of-flight

One of the first observations that we performed to verify that the signal we obtained was consistent with Bragg scattering was a measurement of the decay of the signal in time-of-flight (TOF). Figure 12.2 shows the results for the scattered intensity at $Q = \pi$ and $Q = \theta$ as a function of TOF. The expansion agrees with the expected decay from the Debye-Waller factor of the wavefunctions expanding from the locked $20 E_r$ lattice. For $Q = \pi$, we see enhanced scattering at $\tau = 0$ relative to the uncorrelated cloud ($\tau = 9 \mu\text{s}$), whereas for

$\mathbf{Q} = \theta$, scattering at $\tau = 0$ is reduced. Double occupancies, present in the many-body wavefunction even at low temperatures [55], reduce coherent scattering in all directions, since each spin state scatters with opposite phase and their fields cancel out. For $\mathbf{Q} = \pi$ the coherent enhancement from AFM spin correlations exceeds this reduction. When the Bragg condition is satisfied, the coherent enhancement of the signal along $\mathbf{Q} = \pi$ suppresses the scattered intensity in other directions (there is a sum rule for the total scattered intensity with a fixed \mathbf{k}_{in}), which leads to a further reduction of $I_{\theta 0}$ beyond the reduction due to the presence of doubly occupied sites.

12.3 Numerical calculations

Within the local density approximation (LDA) we model the sample by considering each point in the trap as a homogeneous system in equilibrium at a temperature T , with local values of the chemical potential and the Hubbard parameters determined by the trap potential. The spin structure factor of the sample S_Q can then be expressed as the integral over the trap of the local spin structure factor per lattice site, s_Q .

$$S_Q = a^{-3} N^{-1} \int s_Q(\mu/t, T/t, U/t) d^3\mathbf{r} \quad (12.3)$$

Figure 12.3a shows calculations of s_π at various temperatures in a homogeneous lattice with $U/t = 8$, close to where T_N is maximal[154]. The figure shows that s_π is sharply peaked around $n = 1$ and grows rapidly as T approaches T_N from above.

Figures. 12.3b and 12.3c show, respectively, the results of numerical calculations of the local density and the local spin structure factor in our trap. In Fig. 12.3c we can see that the local spin structure factor is maximized at the largest radius for which the density is $n \approx 1$. The finite extent of the lattice beams causes the lattice depth to decrease with distance from the center, resulting in an increasing t , such that both U/t and T/t decrease with increasing radius for constant T , as shown in Fig. 12.4. The radial decrease in T/t causes $s_\pi(r)$ to maximise at the largest radius for which the density is $n \approx 1$. For large

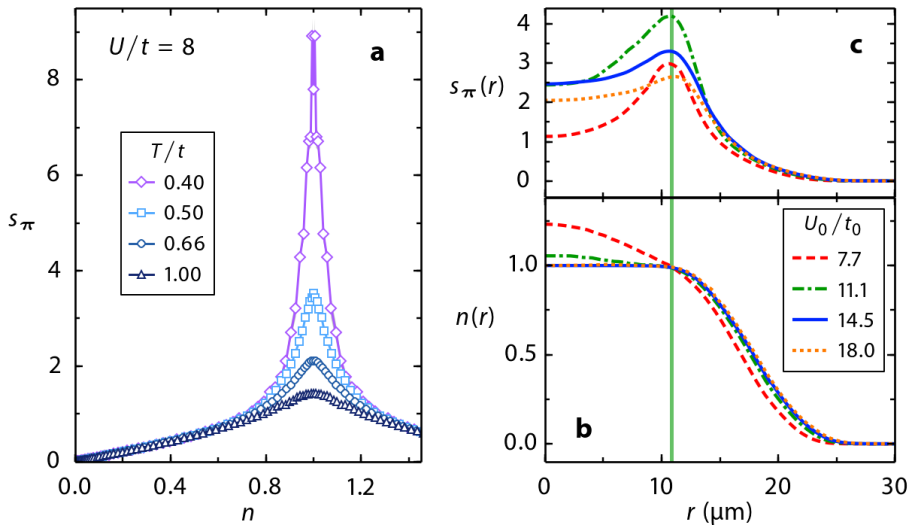


Figure 12.3: Numerical calculations. **a**, DQMC calculation of the spin structure factor per lattice site as a function of density in a homogeneous lattice for several temperatures. s_π is sharply peaked near $n = 1$ and diverges as T approaches T_N . **b**, Density profiles calculated at $T/t_0 = 0.6$ for different U_0/t_0 . The atom number used to obtain each profile maximizes the experimentally measured S_π , as will be explained in §12.4. **c**, Profiles of the local spin structure factor $s_\pi(r)$, for the same conditions as in **b**. The vertical green line in panels **b** and **c** marks the radius at which $s_\pi(r)$ is maximized for $U_0/t_0 = 11.1$.

U_0/t_0 , where the cloud exhibits an $n = 1$ Mott plateau, this is the outermost radius of the plateau.

12.4 Bragg signal optimization

One of the important technical aspects that we encountered with the Bragg signal was the sensitivity to the number of atoms in the trap. In the experiment, we varied the atom number for each value of U_0/t_0 and found that the Bragg signal was sharply peaked. The results of this variation are shown in Fig. 12.5. Beyond optimizing the size and location of the $n = 1$ region of the cloud, according to the picture presented in the previous section, we speculate that the sensitivity of S_π to N may be related with equilibration or adiabaticity in the loading ~~which could depend on atom number~~ ^{process}.

The compensation strength g_0 , which is the same for all U_0/t_0 , was also optimized to

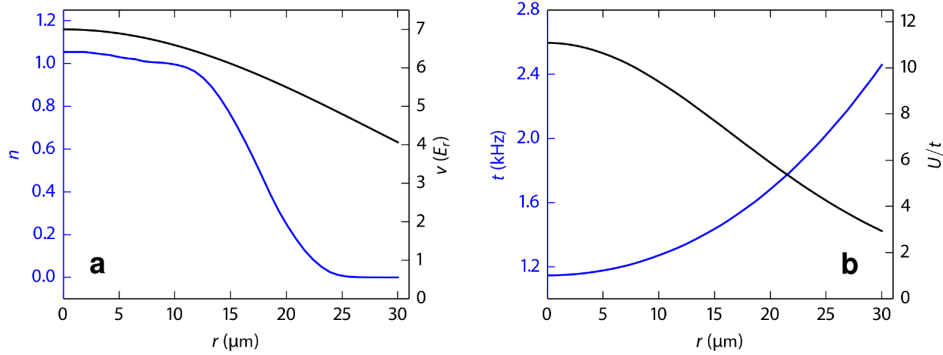


Figure 12.4: **Local variation of the Hubbard parameters.** **a**, The local value of the lattice depth v (black line) is shown as a function of distance from the centre along a body diagonal of the lattice. Due to the finite extent of the lattice beams, v varies across the density profile of the cloud (blue line), which here is calculated for $U_0/t_0 = 11.1$ at $T/t_0 = 0.60$. **b**, The inhomogeneity in v results in spatially varying Hubbard parameters t (blue line) and U/t (black line).

maximize S_π . We found the optimum to be $g_0 = 3.7 E_r$ at a lattice depth $v_0 = 7 E_r$. In a similar way as with the atom number, we believe that the dynamical adjustment of g_0 during the lattice turn-on reduces the time for the system to equilibrate, by minimising the deviation of the equilibrium density distribution in the final potential from the starting density distribution in the dimple trap prior to loading the lattice.

12.5 Spin structure factor

Figure 12.6 shows the measured values of S_π and S_θ at optimal N for various values of U_0/t_0 . We find that S_π is peaked for $10 < U_0/t_0 < 15$. In contrast, the measurements of S_θ vary little over the range of interaction strengths, consistent with an absence of coherent Bragg scattering in this direction. Comparing the measured S_π with numerical calculations for a homogeneous lattice (for example, those in Fig. 12.3a) allows us to set a trap independent upper limit on the temperature, which we determine to be $T/t_0 < 0.7$.

Precise thermometry is obtained by comparing the measured S_π with numerical calculations averaged over the trap density distribution for different values of T . The results of such numerical calculations are ~~also~~ shown in Fig. 12.6, labelled by the value of T/t_* , which

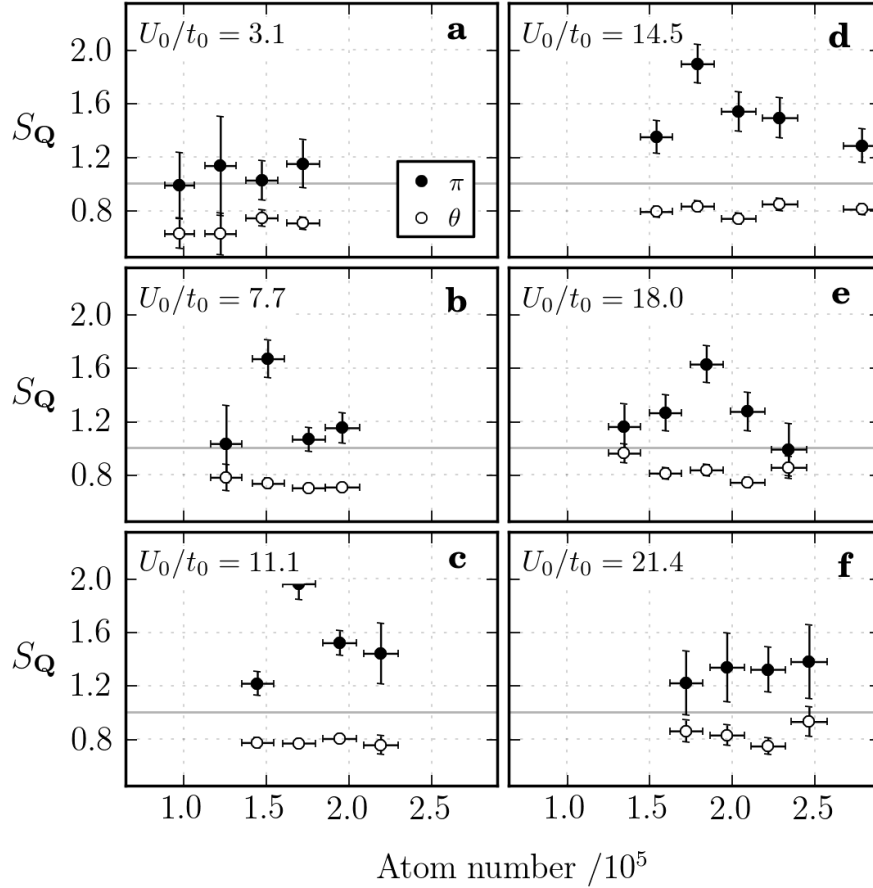


Figure 12.5: Spin structure factor as a function of N . **a-f**, For each U_0/t_0 we vary the atom number N loaded into the lattice and measure S_π and S_θ , (closed and open circles, respectively). We find that S_π depends sensitively on N for all but the lowest and highest values of U_0/t_0 , where S_π is near 1. This sensitivity is consistent with the assumption that only a small volume with $n \simeq 1$ mainly contributes to S_π . The peak in S_π shifts to higher N with increasing U_0/t_0 since the global chemical potential to realize $n = 1$ at the center grows with U_0/t_0 . Vertical error bars represent the standard error of the mean of at least 15 and up to 60 measurements; more measurements were taken at the peak of S_π . Horizontal error bars represent the standard error of the mean of at least 20 measurements of N .

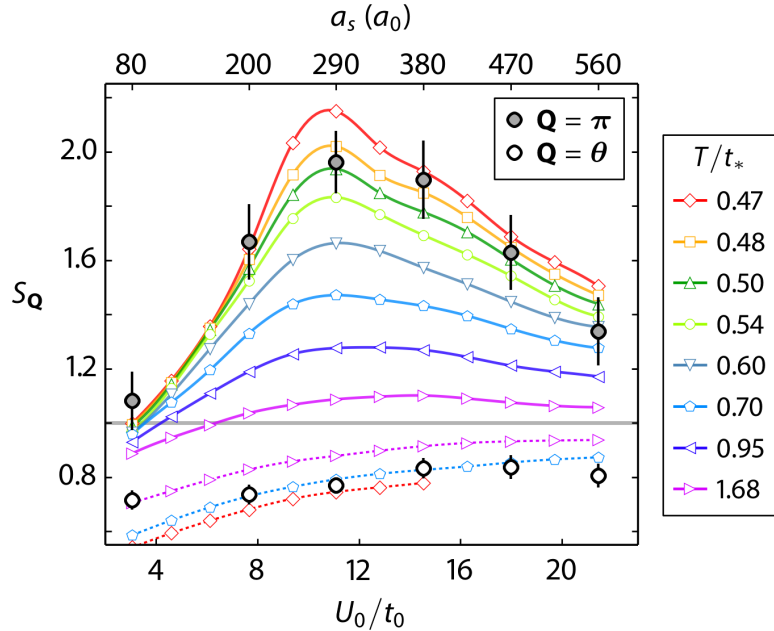


Figure 12.6: **Spin structure factor** Measured S_π (filled circles) and S_θ (open circles) at optimised N (see text) for various U_0/t_0 . The values of the s -wave scattering length corresponding to U_0/t_0 for the experimental points are shown along the top axis. For each point at least 40 *in-situ* and 40 time-of-flight measurements of the scattered intensities are used to obtain the spin structure factor. Error bars are obtained from the SE of the scattered intensities; the raw data for the scattered intensities is shown in Extended Data Fig. 5. Numerical calculations of S_π (open symbols, lines as guide to the eye) and S_θ (open symbols, dashed lines as guide to the eye) for various values of T/t_* . The numerical calculations for S_θ are unreliable for $T/t_* > 0.7$ and $U_0/t_0 > 15$. S_θ decreases slightly for weak interactions, where the fraction of double occupancies increases.

we define as the local value of T/t at the radius where the spin structure factor per lattice site is maximal (see Fig. 12.3a).

At $U_0/t_0 = 11.1$, where measured AFM correlations are maximal, we find $T/t_* = 0.51 \pm 0.06$, where the uncertainty is due to the statistical error in the measured S_π and the systematic uncertainty in the lattice parameters used for the numerical calculation. This temperature is consistent with the data at all values of U_0/t_0 . We caution, however, that for values of $U/t > 10$ a single-band Hubbard model may not be adequate, as corrections involving higher bands may become non-negligible[69, 155] (refer to Fig. 2.10).

As was shown in Fig. 12.3c, for $U_0/t_0 = 11.1$ the dominant contribution to S_π comes

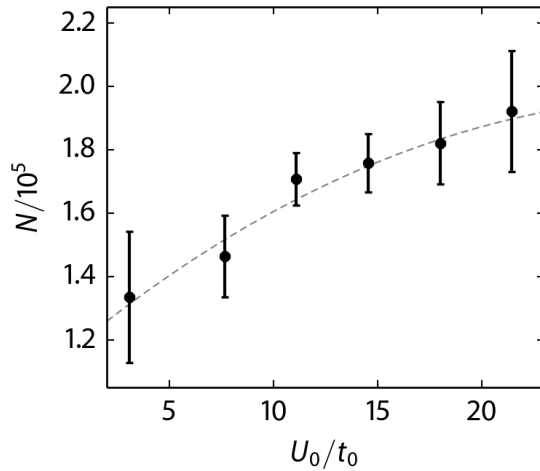


Figure 12.7: **Atom number for the data in Fig. 12.6.** Atom number N which maximises S_π as a function of U_0/t_0 . We control N by adjusting the depth of the dimple trap. Using a linear calibration between the depth of the dimple trap and the final atom number we obtain the value of N corresponding to the data in Fig. 4. The error bars correspond to the standard deviation of the dimple depths used in at least 40 *in-situ* and 40 time-of-flight realisations of the experiment, corresponding to the data in Fig. 4. The line is a third order polynomial fit, which is used to interpolate the value of N for numerical calculations shown in Fig. 4.

from the outermost radius of the Mott plateau. At that radius, the local value of U/t is $U_*/t_* = 9.1$, consistent with DQMC calculations for the homogeneous lattice [154, 54, 156], which find T_N to be maximised for U/t between 8 and 9. For $U_0/t_0 = 11.1$, $t_* = 1.3$ kHz, so we can infer the temperature of the system to be $T = 32 \pm 4$ nK. In terms of T_N , the temperature is $T/T_N = 1.42 \pm 0.16$. At this temperature, the numerical calculations indicate that the correlation length is approximately equal to the lattice spacing.

12.5.1 Atom number

The global chemical potential μ_0 must be increased for larger U_0/t_0 to guarantee the formation of a Mott plateau in the trap. A larger μ_0 results in larger atom number. As we explained above, N is adjusted to maximise the Bragg signal for each experimental value of U_0/t_0 shown in Fig. 12.6. The value of N corresponding to each U_0/t_0 data point in Fig. 12.6 is shown in Fig. 12.7.

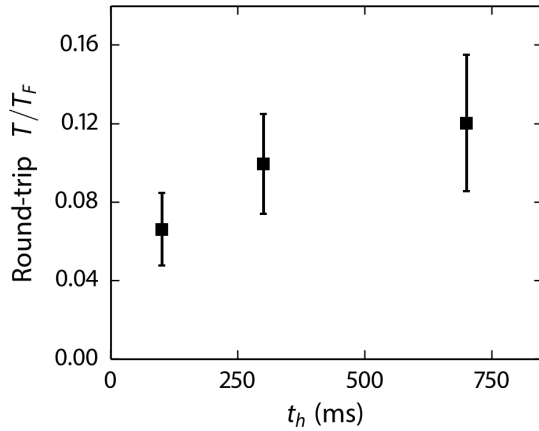


Figure 12.8: **Round-trip temperature measurements.** Measurement of the round-trip T/T_F vs. hold time t_h in a compensated lattice with $v_0 = 7 E_r$ and $g_0 = 3.7 E_r$. The duration of the loading ramps is not included in t_h . The scattering length is $326 a_0$, which corresponds to $U_0/t_0 = 12.5$. Error bars are the standard deviation of 6 independent realisations. The temperature in the dimple trap before loading into the lattice is $T/T_F = 0.04 \pm 0.02$.

12.5.2 Decay of Bragg signal with hold time in the lattice

SIT

To probe the dependence of the spin structure factor on the temperature of the sample we simply wait for a hold time t_h in the lattice before shining the Bragg probe. We measure the temperature in the dimple trap after a lattice round-trip, where we load the atoms into the lattice and then reverse the lattice loading ramps after a hold time t_h . The round-trip temperature measurements help us establish that the sample heats up in the lattice by an amount proportional to t_h , as shown in Fig. 12.8.

SIT

As expected for a system with larger temperature, the spin structure factor decays for longer values of t_h . The results are shown in Fig. 12.9.

12.5.3 Entropy

In Fig. 12.6 we compare the experimental results at various U_0/t_0 with calculations at constant T . Since ultracold atoms are isolated systems, a constant value of the overall

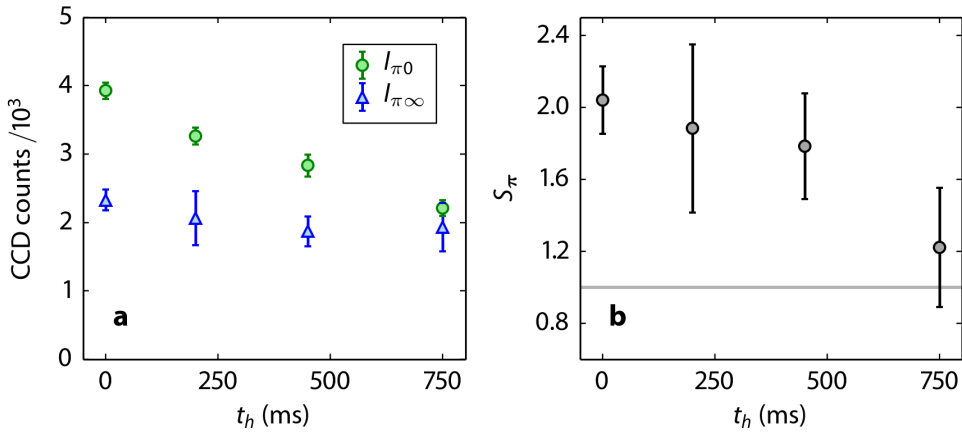


Figure 12.9: Bragg signal decay with hold time. **a**, Detected counts vs. t_h , measured for momentum transfer $\mathbf{Q} = \pi$ for an *in-situ* sample ($I_{\pi0}$, green circles) and after decay of the Debye-Waller factor ($I_{\pi\infty}$, blue triangles). For longer hold times, Bragg scattered intensity $I_{\pi0}$ decays to match $I_{\pi\infty}$, reflecting the absence of AFM correlations in a sample at higher T . **b**, The spin structure factor corresponding to the scattered intensities shown in **a**. For these measurements the scattering length is $200 a_0$, corresponding to $U_0/t_0 = 7.7$ in a $7 E_r$ deep lattice. The compensation is $g_0 = 4.05 E_r$, different from that used for the data in Fig. 4. The increased compensation requires a larger atom number to realise an $n \simeq 1$ shell in the cloud. The atom number used here is 2.6×10^5 atoms. The duration of the Bragg probe is $2.7 \mu\text{s}$ for these data. Error bars in **a** are the standard error of the mean of at least 5 measurements for $I_{\pi\infty}$ and at least 10 measurements for $I_{\pi0}$. Error bars in **b** are obtained from the uncertainty of the measured intensities.

entropy per particle $S/(Nk_B)$ may be more appropriate. We find, from the results of numerical calculations, that over the range $10 < U_0/t_0 < 15$, where AFM correlations are largest, $S/(Nk_B)$ does not vary significantly with U_0/t_0 , at constant T . This is shown in Fig. 12.10, where we plot the entropy per particle $S/(Nk_B)$ corresponding to the constant T calculations in Fig. 12.6.

The calculations show that the entropy per particle in the trap for the range of U_0/t_0 where S_π is maximized, is $S/(Nk_B) \simeq 0.43$, where k_B is the Boltzmann constant. This entropy range is consistent with $T/T_F = 0.04 \pm 0.02$ measured in the harmonic dimple trap before loading the atoms into the lattice[116] and thus justifies the assumption of adiabatic loading.

*for this comparison
 In any case,
 for*

*The fact that the entropy at constant T of all
 factors significantly with w_f, justifies the
 assumption of adiabatic loading.*

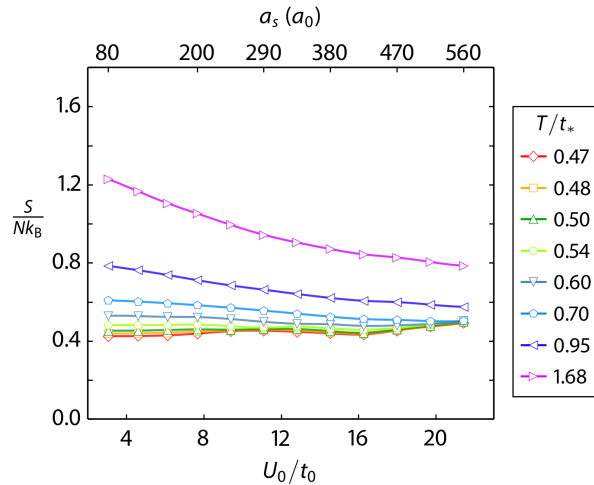


Figure 12.10: **Entropy per particle at constant T .** Overall entropy per particle $S/(Nk_B)$ as a function of U_0/t_0 for the calculations at various T/t_* shown in Fig. 4 (lines are guides to the eye). For the lowest temperatures, $S/(Nk_B)$ does not vary significantly over the range of U_0/t_0 covered by the experiment justifying the treatment at constant T . A value of $S/(Nk_B) \simeq 0.43$ is obtained for the temperature determined from the data in Fig. 4. This entropy is consistent with $T/T_F \simeq 0.04$, measured in the harmonic dimple trap before loading the atoms into the lattice.

12.6 Summary

We have observed AFM correlations in the Hubbard model using ultracold atoms in an optical lattice via spin-sensitive Bragg scattering of light. Because magnetic order is extremely sensitive to T in the vicinity of T_N , Bragg scattering provides precise thermometry in regimes previously inaccessible to quantitative temperature measurements.

In future studies our experimental setup can be configured to study the 2D Hubbard model in an array of planes. Further progress to lower temperature will put us in a position to answer questions about competing pairing mechanisms in 2D, and ultimately resolve the long standing question of d -wave superconductivity in the Hubbard model.

13. Conclusion

I feel very proud to be the first student that will receive a Ph.D. for work done in this apparatus. We started out in 2007 and have always battled more than what would seem necessary to get the experiment up and running. Luckily, we were able to change some problems into opportunities, and now the results of our efforts have paid off.

The low atom numbers that we would achieve in the ODT when loading it directly from the red MOT, led us to focus our efforts on the UVMOT, which was the subject of my Master's thesis. The UVMOT is basically what gives this experiments its edge; it works much better than anybody ever expected (except perhaps Randy). The 323 nm power necessary to operate it is not too high, and it barely needs any repump light. The UVMOT allows us to load a significant number of atoms (10^7) into an ODT with a very moderate depth ($300 \mu\text{K}$, moderate for lithium standards) which is sufficient for the experiments that we carry out.

It was only until my fifth year in grad school (Fall 2011) that we started building up the compensated lattice. We first observed Bragg scattering from the (0 1 0) planes in the summer of 2012. That moment was an important turning point, from then on most of our time was no longer spent building something new for the apparatus but actually running experiments.

The last two years have been almost fully dedicated to achieving our goal of measuring the spin structure factor in the lattice using Bragg scattering of light. Somehow everybody thought that the Bragg signal would be like a beacon, but we soon realized that we were looking for a needle in a haystack. We were forced to rely heavily on statistics to bring the AFM correlations signal out of the background. The complications with the signal to

noise ratio led to my efforts in understanding the Bragg scattering measurement in the limit where the signal is just above the incoherent scattering background. Furthermore, in order to consolidate our results, we saw the need to collaborate closely with theorists. I quickly realized how little I new about the Hubbard model which I had been trying to realize experimentally, but I saw here another opportunity to serve as the bridge between the theoretical results and our experimental measurements.

Understanding the theoretical results available for the Hubbard model, and implementing the local density approximation has led to the possibility of using Bragg scattering as a thermometer for atoms in a lattice. This is a technique that we hope will be useful for other groups. In our apparatus we hope to continue perfecting the measurement of AFM correlations and use it as a guiding light to find ways of squeezing more entropy out of the system and bring it closer to realizing the full potential of quantum simulation. Studying pairing may not be so far after all, given that some entropy can be squeezed out of the system by increasing the lattice depth along one of the axis, which would create a set of uncorrelated two-dimensional (2D) planes, each one an independent realization of the 2D Hubbard model. As was already shown for 1D chains [45], when you have a fixed amount of entropy in the total system you can “divide and conquer”. The big challenge then would be figuring out how to obtain information about the 2D systems in our setup, given that Bragg scattering as presented here, would not work between the uncorrelated planes. Nevertheless, the 3D system can be used in that case solely for the purpose of thermometry.

In the near future, our experiment will undergo a significant upgrade to a new compensated optical lattice setup. The setup has been carefully designed to implement the ideas that were presented in Chapter 5 of this thesis. It also boasts superior mechanical stability, which we hope will eliminate the need to realign the compensated lattice every day.

In the near future, there are also plans to explore physics in one dimension (1D) using our apparatus. This geometry can be created in our system by simply turning off one of the lattice beams, giving rise to an array of one-dimensional (1D) tubes. The physics of

1D systems provides an interesting test-bed for quantum simulation, since exact solutions exist for the many-body problem in 1D.

I believe that it is a good idea for the apparatus to diversify and try to study systems for which the temperature requirements are not as low as in the strongly correlated regime of the 3D Hubbard model. The 1D systems mentioned above are one example, but also there are a lot of interesting possibilities such as studying the Hubbard model with attractive interactions or also trying to develop techniques to study the dynamics of systems out of equilibrium.

The apparatus has finally reached maturity. It is a versatile machine, capable of producing some the coldest degenerate Fermi gases of ultracold atoms ever recorded. I hope that the new generations of graduate students that come to it have as much fun as I did trying to figure things out.

B. Numerical calculations for the Hubbard Hamiltonian in the compensated lattice

In this appendix we present the results of numerical calculations for a homogenous Hubbard model in a simple cubic lattice, which serve as the basis for our implementation of the local density approximation (LDA). As we mentioned in Chapter 3, our theory collaborators provide us with results of DQMC and NLCE calculations in a grid of U/t , T/t , and μ/t values. The DQMC and NLCE results complement each other. DQMC can provide results at arbitrary chemical potential down to the Néel transition temperature if the coupling is weak, $U/t \leq 9$. For strong coupling DQMC runs into the sign problem, however, NLCE can provide result for arbitrary U/t at temperatures $T > 0.4t$, so we use it for large values of U/t .

In the sections below we present the complete NLCE and DQMC data sets and explain how we use the available data to interpolate the values of the thermodynamic quantities for arbitrary values of U/t , T/t and μ/t .

The full data set, along with more plots and the code used for interpolation are available online at [? ?].

B.1 NLCE

The NLCE data set was provided by E. Khatami. It includes exact results down to $T/t = 1.6$ for a wide range of μ/T , for the following thermodynamic quantities (all quantities are given per lattice site):

- energy
- entropy
- energy fluctuations
- specific heat
- density
- double occupancy
- density fluctuations
- nearest neighbor spin correlations
- S_z fluctuations
- antiferromagnetic structure factor

For temperatures below $T/t = 1.6$, an Euler resummation is performed [96] to obtain estimates of the thermodynamic quantities. At values of the temperature around $T/t = 0.4$ the results start getting very noisy, however we can extract usable data set by applying a low pass filter to the data¹. The original data and the filtered data are shown in Fig. B.1. Larger T/t are not as noisy, as shown for the density in Fig. B.2, but the filter is still used up to $T/t = 1.4$ to remove some spurious points that show up in the data. At $T/t > 1.6$ the data is exact and it has no spurious points.

B.1.1 Complete NLCE data set

B.2 Spin structure factor

Our experiment measures the bulk spin structure factor $\bar{S}_{\mathbf{Q}}$ for an inhomogeneous realization of the Hubbard model. Theoretical approaches such as QMC and NLCE consider a homogeneous system with a finite number of lattice sites L^3 and calculate the structure factor

$$S_{\mathbf{Q}} = \frac{4}{L^3} \sum_{i,j} e^{i\mathbf{Q} \cdot (\mathbf{R}_i - \mathbf{R}_j)} \langle \sigma_{zi} \sigma_{zj} \rangle \quad (\text{B.1})$$

In the local density approximation we can think of every point \mathbf{r} of our lattice site as a homogeneous system for which $S_{\mathbf{Q}}(\mathbf{r})$ can be obtained. We can relate the measured bulk

¹The type of filter used is the Savitzky-Golay filter <http://www.wire.tu-bs.de/OLDWEB/mameyer/cmr/savgol.pdf>

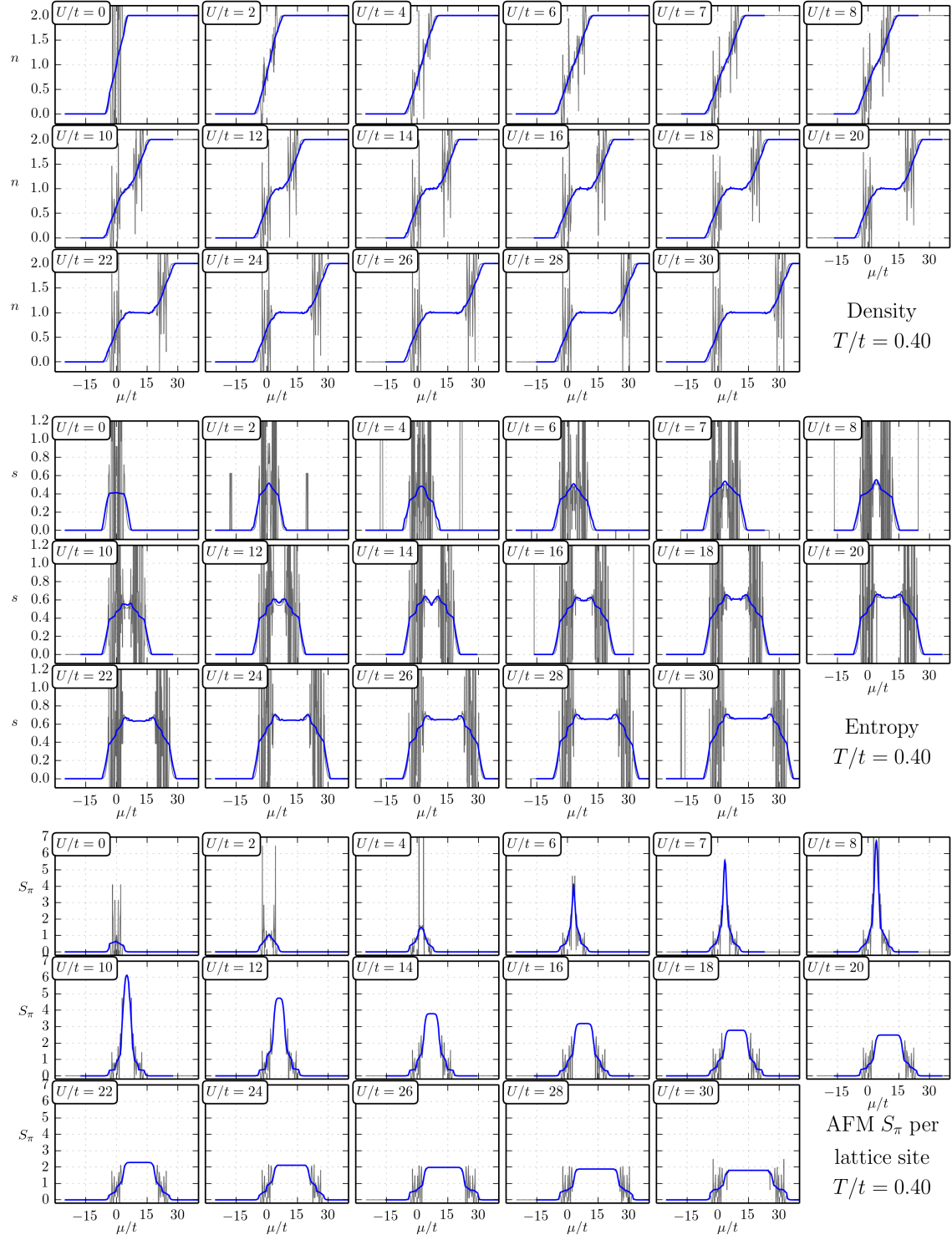


Figure B.1: Lowest temperature data accessible to the NLCE by extrapolation, $T/t = 0.4$. The original data provided by Ehsan is shown in gray and the data after filtering is shown in blue.

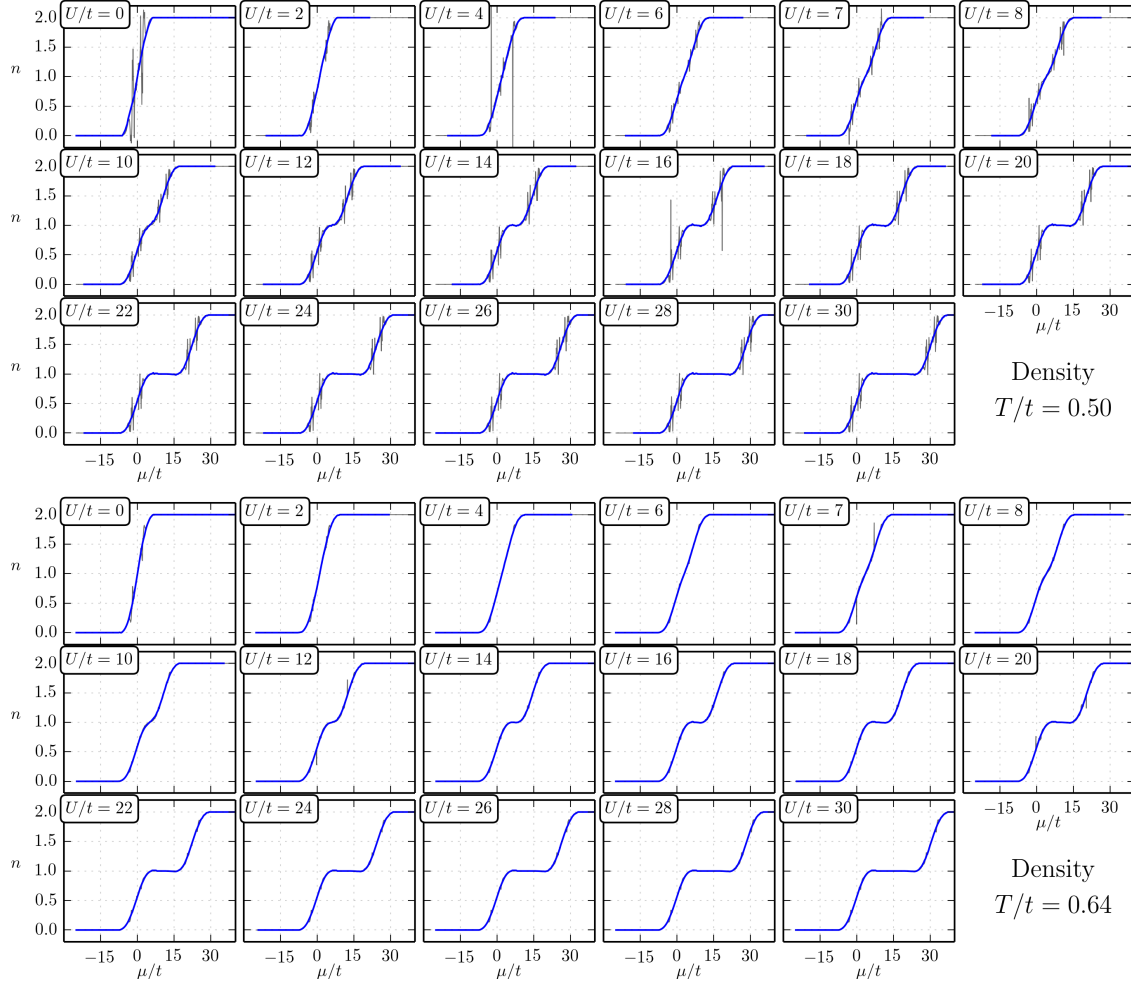


Figure B.2: Larger values of T do not show as much noise as $T/t = 0.4$.

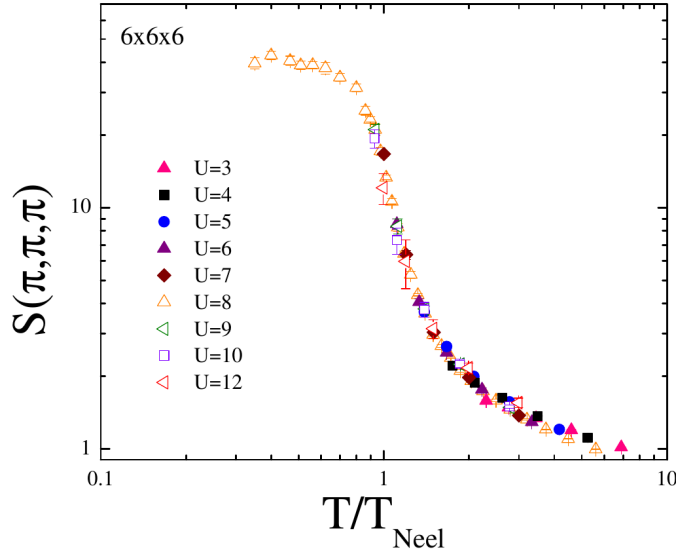
spin structure factor to the local $S_{\mathbf{Q}}(\mathbf{r})$ as

$$\bar{S}_{\mathbf{Q}} = \frac{1}{N} \int S_{\mathbf{Q}}(\mathbf{r}) d^3\mathbf{r} \quad (\text{B.2})$$

The NLCE data provided by Ehsan gives $S_{\mathbf{Q}}$ directly whereas the QMC data provided by Thereza gives $S_{\mathbf{Q}}/n$. To compare with experiment we have decided to use $S_{\mathbf{Q}}/n$ such that

$$\bar{S}_{\mathbf{Q}} = \frac{1}{N} \int \left[\frac{S_{\mathbf{Q}}}{n} \right]_{\mathbf{r}} n(\mathbf{r}) d^3\mathbf{r} \quad (\text{B.3})$$

Also, in our LDA calculations we have assumed that there is spherical symmetry in the


 Figure B.3: S_π vs T/T_N .

system so

$$\bar{S}_Q = \frac{4\pi}{N} \int \left[\frac{S_Q}{n} \right]_{r_d} n(r_d) r_d^2 dr_d \quad (\text{B.4})$$

where r_d is the distance from the origin along a 111 body diagonal of the lattice.

The validity of the spherical symmetry assumption is very questionable, since away from the diagonal the lattice depths are different along the x, y, z directions and an anisotropic Hubbard model should be used. However, for simplicity this is how we decided to treat the system.

B.2.1 Effective fraction

In the current version of the paper we say something along the lines of : “ x percent of the cloud contributes effectively to the observed structure factor”. More formally x , the effective fraction is defined as

$$\bar{S}_\pi - 1 = \frac{x}{100} ([S_\pi]_{\max} - 1) \quad (\text{B.5})$$

where $[S_\pi]_{\max}$ is the maximum value attained by $S_\pi(r_d)$.

We will see later on that the current LDA results (which are still not cold enough to match the experimental data) lead to an effective fraction of 40%. So, for our observed $\bar{S}_\pi = 1.9$ then $[S_\pi]_{\max} = 3.3$, which would imply that the lowest local T/T_N in our cloud is $T/T_N \approx 1.5$ according to QMC calculations by Thereza, cf. Fig. B.3.

So at the moment the best claim we can make is $T/T_N < 1.5$.

B.3 NLCE data

Ehsan has provided us with exact NLCE (numerical linked-cluster expansion) data down to $T/t = 1.6$. Below this temperature he can do a resummation to obtain the thermodynamic quantities. At values of the temperature around $T/t = 0.4$ the results start getting very noisy, however we can recover a usable data set by applying a low pass filter to the data². The original data and the filtered data are shown in Fig. B.1. Larger T/t values are less noisy, but the filter is still used up to $T/t = 1.4$ to remove some spurious points that show up in the data. At $T/t > 1.6$ the data is exact and it has no spurious points.

We can use the NLCE data to see that the density as a function of chemical potential is pretty much frozen for $T/t < 1.0$, see Fig. B.4. The high temperature series expansion (HTSE) that I was using before to calculate density profiles works down to about $T/t \approx 1.6$, so I was unable to capture the “Mottness” of the density profile as we see it in the experiment.

The data for S_π/n provided by NLCE is shown in Fig. B.5. Notice that to avoid errors when dividing by a small value of n we have decided to enforce $S_\pi = 1$ for densities less than a density cutoff. The density cutoff is adjusted for each value of U/t .

²The type of filter used is the Savitzky-Golay filter <http://www.wire.tu-bs.de/OLDWEB/mameyer/cmr/savgol.pdf>

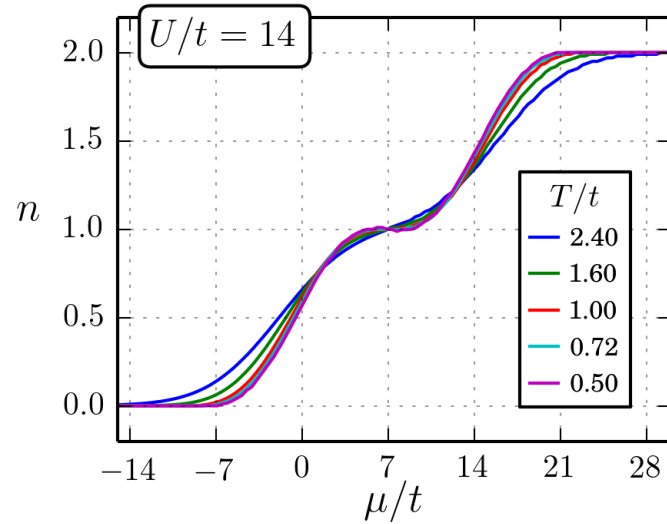


Figure B.4: NLCE data at $U/t = 14$. For $T/t \leq 1$ the density does not show much variation.

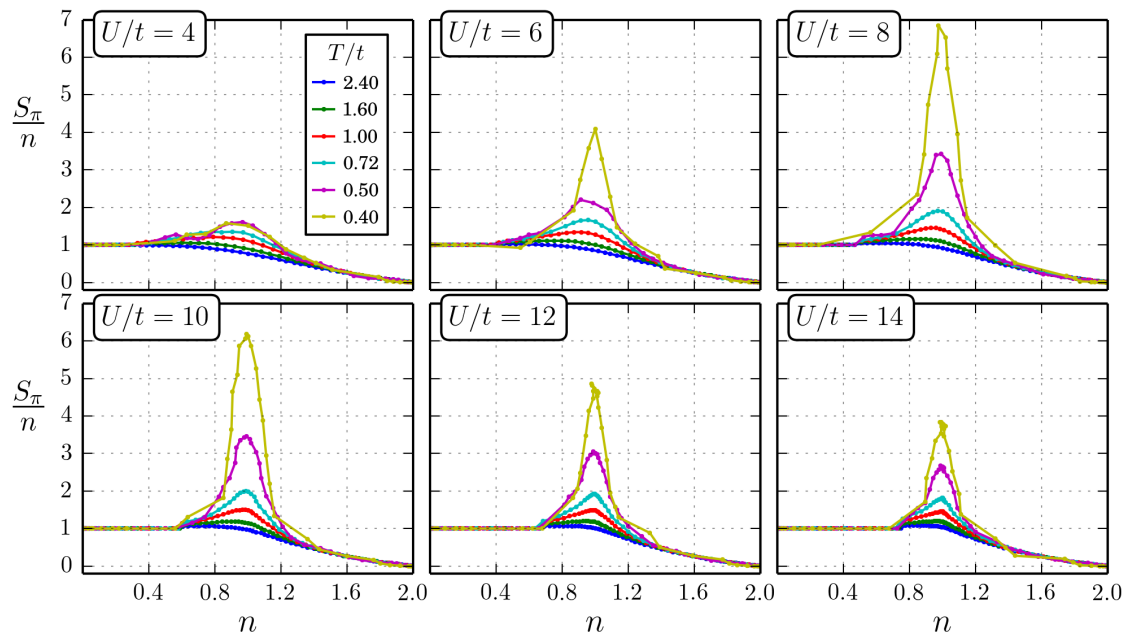


Figure B.5: NLCE S_π/n data for various interactions and temperatures.

B.4 QMC data

The QMC data does not suffer from noise problems for small values of T/t , however there is much less of it available. Fig. B.6 shows the available U/t and T/t values. The entropy and double occupancy, not shown in the Figure are also available from Thereza's data set, as well as the structure factor in the θ direction.

B.5 NLCE data and QMC data comparison

In Fig. B.7 we show QMC and NLCE data sets on the same plot. A direct comparison is possible at $U/t = 6$. The QMC data at $U/t = 7$ is compared with NLCE at $U/t = 8$ which reveals that the NLCE structure factor is perhaps too broad as a function of n . It is clear from this plots that the density is frozen for $T/t < 1.0$ and that both QMC and NLCE have very good agreement on the density.

B.6 Comparison of experimental data with LDA

The way we will proceed is as follows:

1. Set up a trap geometry based on our experimental calibration. The trap geometry determines the local chemical potential, the local U/t and the local T/t .
2. Use the NLCE data to find the global chemical potential that produces the desired atom number N . The temperature used simply needs to be $T/t < 1.0$, since $n(\mu)$ is frozen below this temperature.
3. For the local S_π/n determination, set a value of $[T/t]_0$. This is the local value of T/t at the center of the trap. Use the global chemical potential (from 2) along with the local U/t and T/t to get the local S_π/n via interpolation from available QMC and NLCE data.

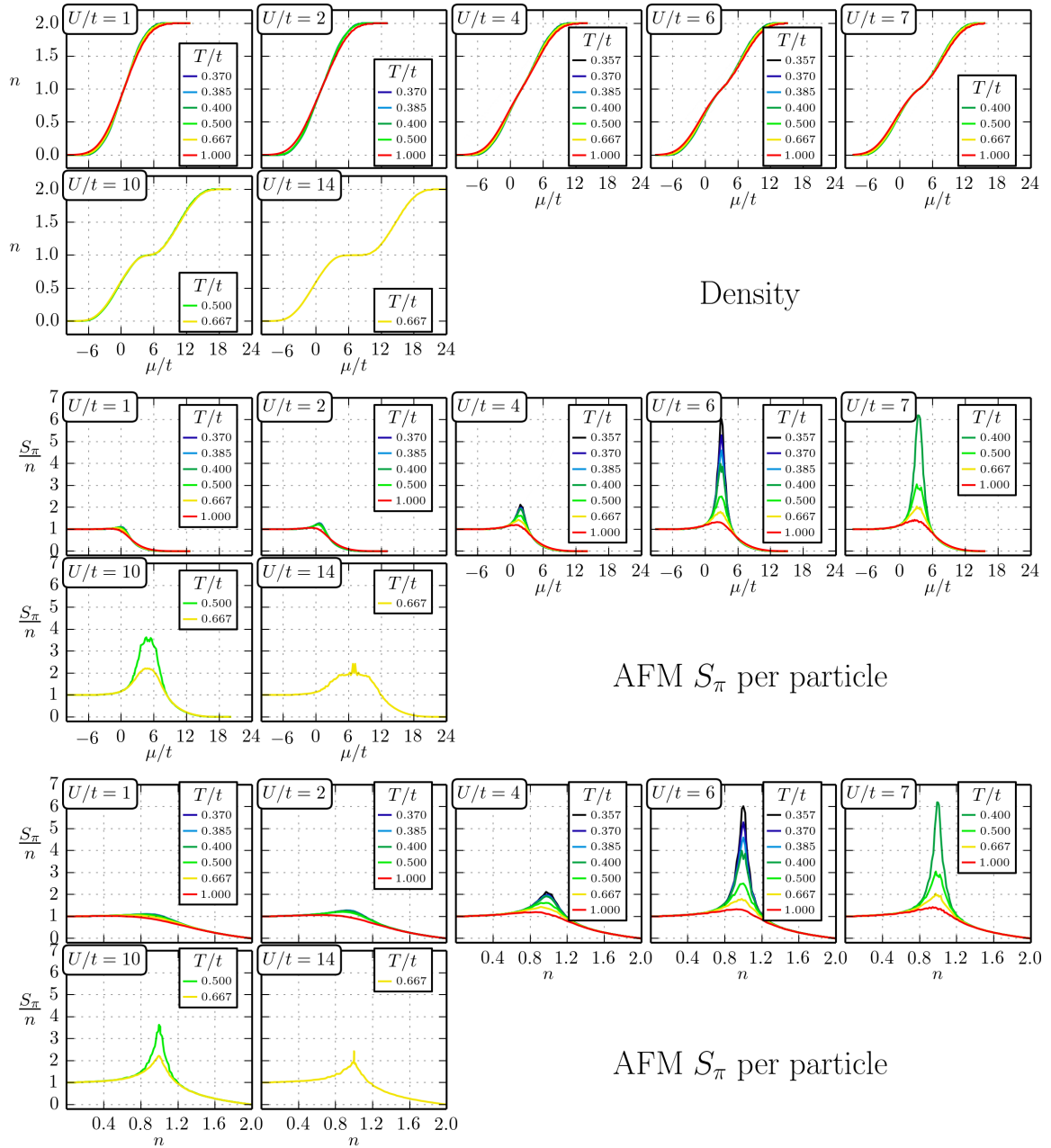


Figure B.6: All available QMC data for the density, S_π and S_π/n . Entropy, double occupancy and S_θ/n are available but not shown here.

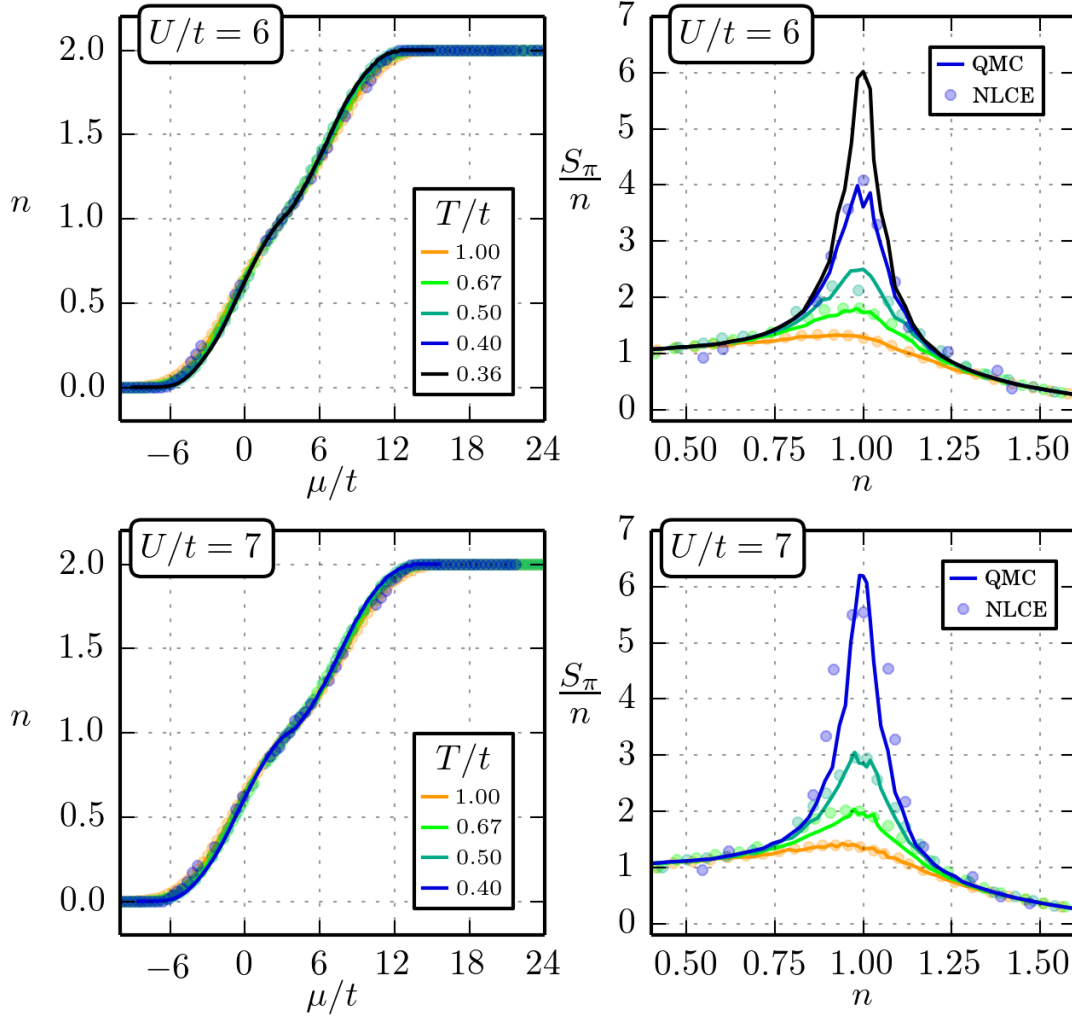


Figure B.7: Comparison between QMC and NLCE data. At $U/t = 6$ both methods have data available whereas the QMC data at $U/t = 7$ is compared with the NLCE data at $U/t = 8$.

4. Integrate the local S_π/n over the trap to obtain the bulk spin structure factor \bar{S}_π .
5. Repeat 3 and 4 for decreasing values of $[T/t]_0$ until the resulting \bar{S}_π agrees with the experimental measurement.

B.6.1 Determination of Spi/n by interpolation

We use a combination of the available QMC and NLCE data set to find out S_π/n for given local values of μ/t , U/t , and T/t . To allow evaluation for arbitrary values of the

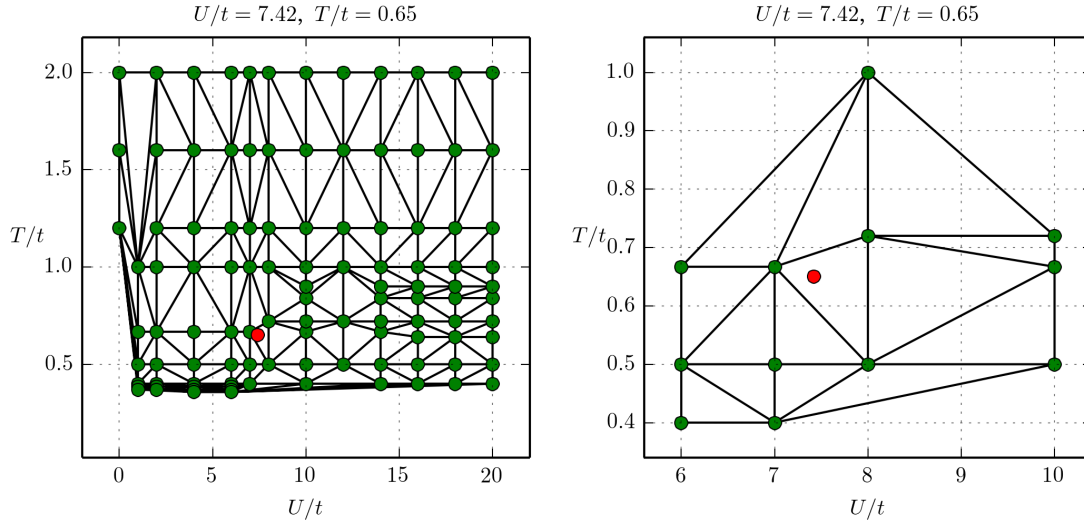


Figure B.8: Illustration of linear interpolation. Left panel shows all available points from a combination of QMC and NCE data sets. Right panel shows a close up view and the triangulation scheme which is used to linearly interpolate. The value at the red point is determined by the 3 green points which form the triangle that enclose it. Note that the value of S_π/n at each green point is obtained from the data tables at the local chemical potential of interest.

parameters we interpolate linearly between the available data points. An example is shown in Fig. B.8.

B.6.2 LDA density profiles with NLCE data, dependence on T

To illustrate the effect of temperature on the density profile we show in Fig. B.9 density profiles with $n = 1$ at the center, calculated for various values of $[T/t]_0$, where $[T/t]_0$ is the local value of T/t at the center of the cloud. The sample is assumed to be isothermal so it has constant T throughout, the local value of t varies due to the size of the lattice beams. As expected we see that for $[T/t]_0 < 1$ the density profile does not change very much, which validates our approach of calculating the density profile and determining the global chemical potential at a single $T/t < 1.0$ using the NLCE data (see step 2 in the prescription outlined above).

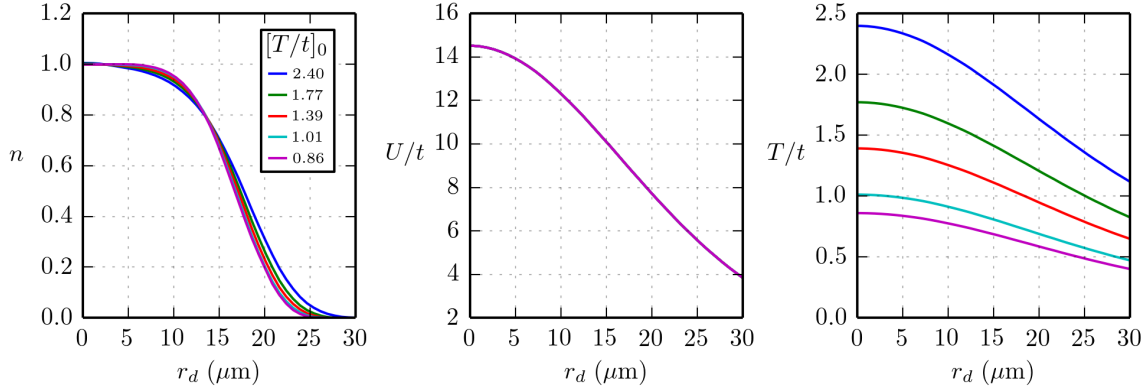


Figure B.9: Density profiles with $n = 1$ at the center for various values of $[T/t]_0$. For $[T/t]_0 < 1$ the density profile changes very little with temperature. The right two panes show the spatial variation of U/t and T/t across the sample, illustrating the degree of inhomogeneity in the system.

B.6.3 LDA S_π/n profiles, lowest accessible T variation of N

In the experiment we varied the atom number to maximize the Bragg signal for a given value of $[U/t]_0$. Here we calculate S_π profiles for various atom numbers and show how does the bulk spin structure factor \bar{S}_π varies with atom number.

The results for the lowest accessible values of $[T/t]_0$ are shown in Figs. B.10-B.13. Even though there is data available down to $T/t = 0.36$ the lowest accessible $[T/t]_0$ is only 0.68 because as one moves radially outwards the local T/t decreases. We are limited by the local value of T/t at the edge of the cloud.

Notice that in Figs. B.10-B.13 we indicate values for $[T/t]^*$ and $[U/t]^*$, which are the local values of T/t and U/t where S_π/n is maximized.

The main features that stand out from Figs. B.10-B.13 are

1. Looking at weak interactions ($[U/t]_0 = 7.6$) we see that the peak in \bar{S}_π as a function of N is much broader than what we have observed in the experiment.
2. Looking at strong interactions ($[U/t]_0 \geq 14.5$) we see that \bar{S}_π continues to increase with atom number. For larger atom numbers the contribution to the structure factor

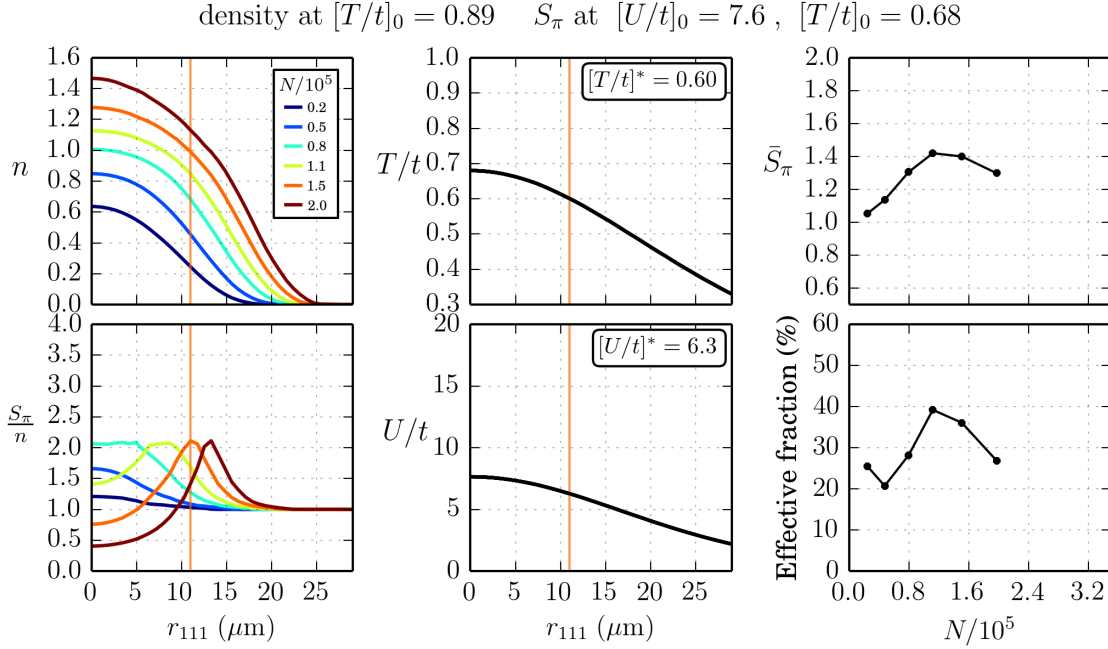


Figure B.10: Scattering length $200 a_0$ ($[U/t]_0 = 7.6$). Variation of density profile, S_π/n profile, \bar{S}_π and effective fraction with atom number.

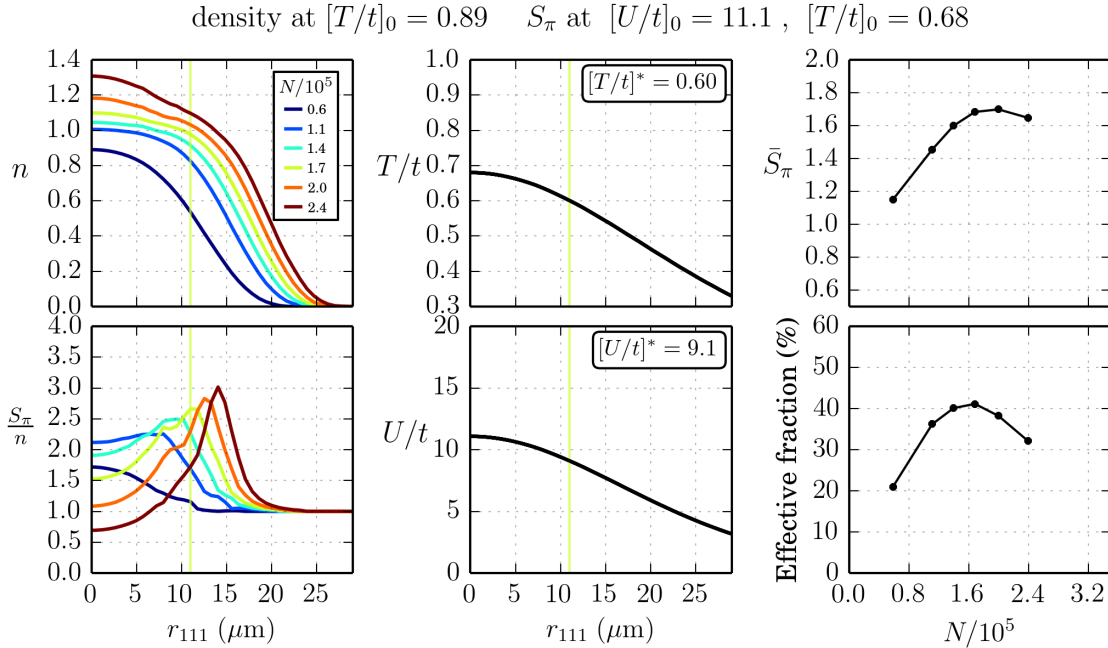


Figure B.11: Scattering length $290 a_0$ ($[U/t]_0 = 11.1$).

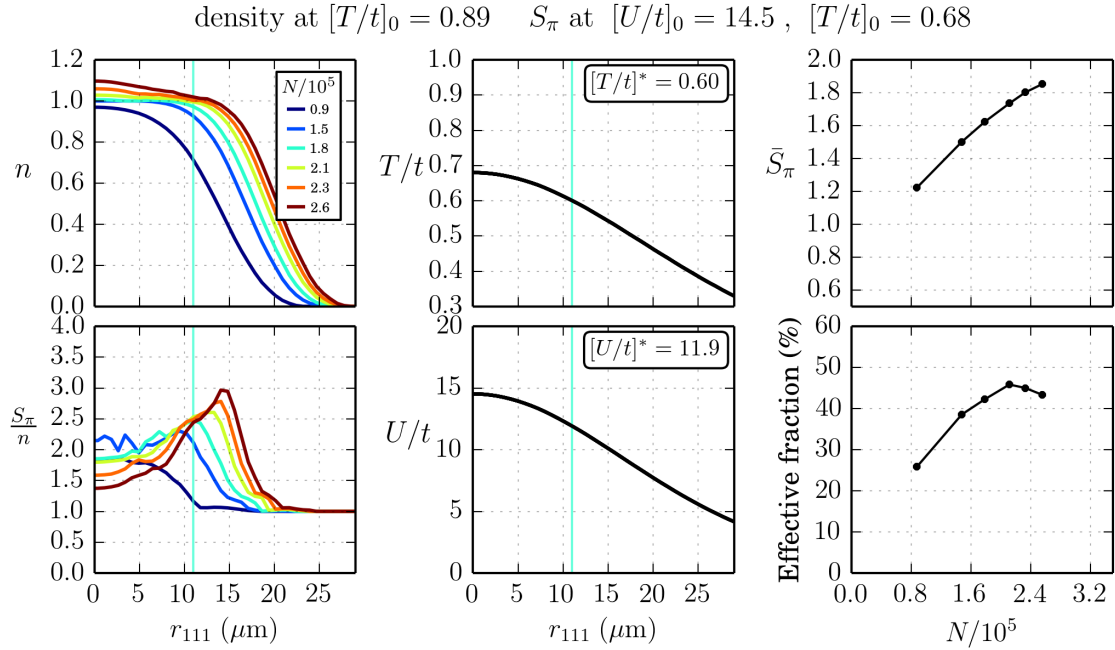


Figure B.12: Scattering length $380 a_0$ ($[U/t]_0 = 14.5$).

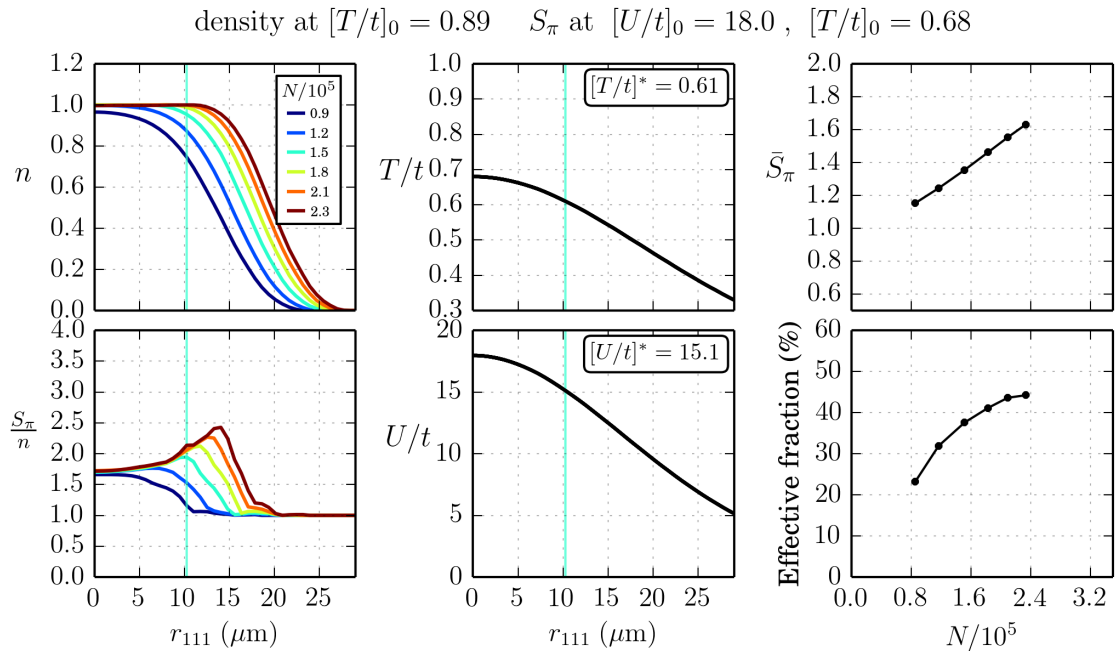


Figure B.13: Scattering length $470 a_0$ ($[U/t]_0 = 18.0$).

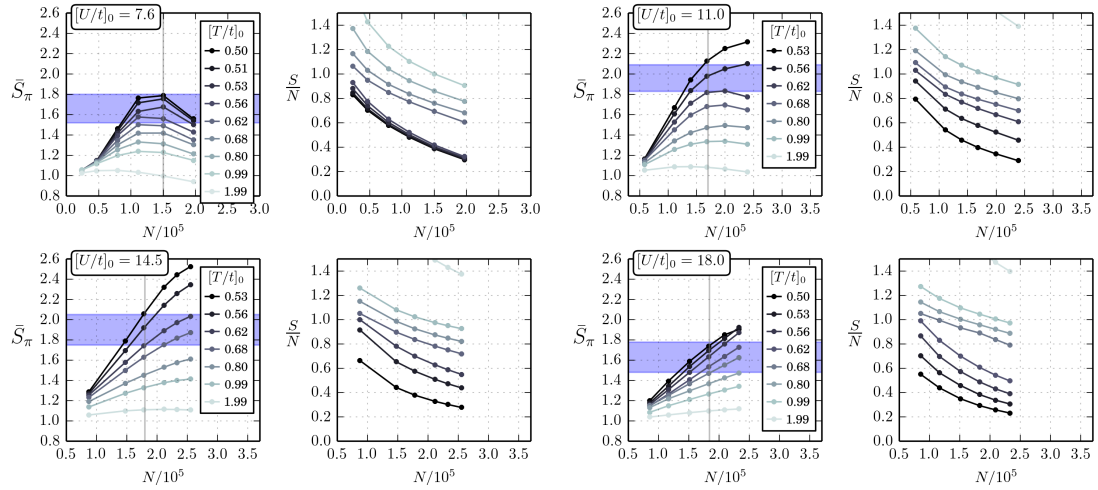


Figure B.14: Final comparison of experimental data with LDA. The shaded blue area indicates the experimental range for \bar{S}_π . The vertical gray line indicates the atom number at which the Bragg signal peaks up in the experiment. For larger atom numbers the spherical symmetry assumed in the LDA comes into question. We see that the lowest temperature accessible at the moment, $[T/t]_0 = 0.68$, is not cold enough to reproduce the \bar{S}_π observed in the experiment for $[U/t]_0 \leq 14.4$. In the case of $[U/t]_0 = 17.9$ at the value of N relevant for the experiment (vertical gray line) the LDA at $[T/t]_0 = 0.68$ just touches the experimental error bar.

is coming from the outermost shell of the cloud. We are afraid that our spherical symmetry assumption may not apply as far out from the center and that \bar{S}_π should ultimately decay with increasing atom number, as we observe in the experimental data.

B.6.4 \bar{S}_π vs. N for various T 's

Finally we repeat calculations like those shown in Figs. B.10-B.13 for several temperatures and show the results for \bar{S}_π in Fig. B.14. Some comments are included in the figure caption.

BIBLIOGRAPHY

- [1] X. Wen, *Quantum Field Theory of Many-Body Systems: From the Origin of Sound to an Origin of Light and Electrons, Oxford Graduate Texts* (OUP Oxford, 2004). 1
- [2] A. Altland and B. Simons, *Condensed Matter Field Theory* (Cambridge University Press, 2010). 2
- [3] N. Ashcroft and N. Mermin, *Solid state physics* (Saunders College, 1976). 2, 35
- [4] L. Landau, *Collected papers of L. D. Landau* (Gordon and Breach, 1965). 2
- [5] K. Andres, J. E. Graebner, and H. R. Ott, “4f-Virtual-Bound-State Formation in CeAl₃ at Low Temperatures,” Phys. Rev. Lett. **35**, 1779–1782 (1975). 2
- [6] F. Steglich, J. Aarts, C. D. Bredl, W. Lieke, D. Meschede, W. Franz, and H. Schäfer, “Superconductivity in the Presence of Strong Pauli Paramagnetism: CeCu₂Si₂,” Phys. Rev. Lett. **43**, 1892–1896 (1979). 2
- [7] D. C. Tsui, H. L. Stormer, and A. C. Gossard, “Two-Dimensional Magnetotransport in the Extreme Quantum Limit,” Phys. Rev. Lett. **48**, 1559–1562 (1982). 2
- [8] R. B. Laughlin, “Anomalous Quantum Hall Effect: An Incompressible Quantum Fluid with Fractionally Charged Excitations,” Phys. Rev. Lett. **50**, 1395–1398 (1983). 2, 3
- [9] J. Bednorz and K. Müller, “Possible high- T_c superconductivity in the Ba-La-Cu-O system,” Zeitschrift für Physik B Condensed Matter **64**, 189–193 (1986). 2
- [10] P. Coleman, “Many Body Physics: Unfinished Revolution,” in *International Conference on Theoretical Physics*, D. Iagolnitzer, V. Rivasseau, and J. Zinn-Justin, eds., (Birkhäuser Basel, 2004), pp. 559–580. 2

- [11] P. W. Anderson, “More Is Different,” *Science* **177**, 393–396 (1972). 2
- [12] X. Wen, “Topological orders in rigid states,” *International Journal of Modern Physics B* **04**, 239–271 (1990). 3
- [13] J. A. Hertz, “Quantum critical phenomena,” *Phys. Rev. B* **14**, 1165–1184 (1976). 3
- [14] S. Sachdev, *Quantum Phase Transitions, Quantum Phase Transitions* (Cambridge University Press, 2011). 3
- [15] “The Hubbard model at half a century,” *Nature Physics* **9**, 523–523 (2013). 4
- [16] J. Hubbard, “Electron Correlations in Narrow Energy Bands. III. An Improved Solution,” *Proceedings of the Royal Society of London. Series A, Mathematical and Physical Sciences* **281**, pp. 401–419 (1964). 4, 37
- [17] J. Quintanilla and C. Hooley, “The strong-correlations puzzle,” *Physics World* **22**, 32–37 (2009). 5
- [18] D. Jaksch, C. Bruder, J. I. Cirac, C. W. Gardiner, and P. Zoller, “Cold Bosonic Atoms in Optical Lattices,” *Phys. Rev. Lett.* **81**, 3108–3111 (1998). 5
- [19] R. P. Feynman, “Simulating physics with computers,” *International journal of theoretical physics* **21**, 467–488 (1982). 5
- [20] M. Greiner, O. Mandel, T. Esslinger, T. Hänsch, and I. Bloch, “Quantum phase transition from a superfluid to a Mott insulator in a gas of ultracold atoms,” *Nature* **415**, 39–44 (2002). 5
- [21] N. Gemelke, X. Zhang, C.-L. Hung, and C. Chin, “In situ observation of incompressible Mott-insulating domains in ultracold atomic gases.,” *Nature* **460**, 995–8 (2009). 5, 184
- [22] K. Jiménez-García, R. L. Compton, Y.-J. Lin, W. D. Phillips, J. V. Porto, and I. B. Spielman, “Phases of a Two-Dimensional Bose Gas in an Optical Lattice,” *Physical Review Letters* **105**, 110401 (2010).

- [23] S. Trotzky, L. Pollet, F. Gerbier, U. Schnorrberger, I. Bloch, N. V. Prokof'ev, B. Svistunov, and M. Troyer, "Suppression of the critical temperature for superfluidity near the Mott transition," *Nature Physics* **6**, 998–1004 (2010).
- [24] M. J. Mark, E. Haller, K. Lauber, J. G. Danzl, a. J. Daley, and H.-C. Nägerl, "Precision Measurements on a Tunable Mott Insulator of Ultracold Atoms," *Physical Review Letters* **107**, 175301 (2011).
- [25] X. Zhang, C.-L. Hung, S.-K. Tung, and C. Chin, "Observation of quantum criticality with ultracold atoms in optical lattices," *Science (New York, N.Y.)* **335**, 1070–2 (2012). 5
- [26] J. K. Freericks and H. Monien, "Phase diagram of the Bose-Hubbard Model," *EPL (Europhysics Letters)* **26**, 545 (1994). 5
- [27] W. Krauth and N. Trivedi, "Mott and Superfluid Transitions in a Strongly Interacting Lattice Boson System," *EPL (Europhysics Letters)* **14**, 627 (1991).
- [28] M. P. A. Fisher, P. B. Weichman, G. Grinstein, and D. S. Fisher, "Boson localization and the superfluid-insulator transition," *Phys. Rev. B* **40**, 546–570 (1989). 5
- [29] T. Fukuhara, P. Schauß, M. Endres, S. Hild, M. Cheneau, I. Bloch, and C. Gross, "Microscopic observation of magnon bound states and their dynamics," *Nature* **502**, 76–9 (2013). 5
- [30] D. Scalapino, "The case for $d_{x^2-y^2}$ pairing in the cuprate superconductors," *Physics Reports* **250**, 329 – 365 (1995). 5
- [31] W. Hofstetter, J. I. Cirac, P. Zoller, E. Demler, and M. D. Lukin, "High-Temperature Superfluidity of Fermionic Atoms in Optical Lattices," *Phys. Rev. Lett.* **89**, 220407 (2002). 5
- [32] Y.-R. Lee, M.-S. Heo, J.-H. Choi, T. T. Wang, C. A. Christensen, T. M. Rvachov, and W. Ketterle, "Compressibility of an ultracold Fermi gas with repulsive interactions," *Phys. Rev. A* **85**, 063615 (2012). 6

- [33] M. Köhl, H. Moritz, T. Stöferle, K. Günter, and T. Esslinger, “Fermionic Atoms in a Three Dimensional Optical Lattice: Observing Fermi Surfaces, Dynamics, and Interactions,” *Physical Review Letters* **94**, 080403 (2005). 6
- [34] R. Jördens, N. Strohmaier, K. Günter, H. Moritz, and T. Esslinger, “A Mott insulator of fermionic atoms in an optical lattice.,” *Nature* **455**, 204–7 (2008). 6, 8, 137, 183
- [35] U. Schneider, L. Hackermüller, S. Will, T. Best, I. Bloch, T. A. Costi, R. W. Helmes, D. Rasch, and A. Rosch, “Metallic and insulating phases of repulsively interacting fermions in a 3D optical lattice.,” *Science (New York, N.Y.)* **322**, 1520–5 (2008). 6, 8, 137, 183
- [36] A. Damascelli, Z. Hussain, and Z. Shen, “Angle-resolved photoemission studies of the cuprate superconductors,” *Reviews of Modern Physics* **75** (2003). 6
- [37] R.-H. He *et al.*, “From a single-band metal to a high-temperature superconductor via two thermal phase transitions.,” *Science (New York, N.Y.)* **331**, 1579–83 (2011). 6
- [38] K. Jin, N. P. Butch, K. Kirshenbaum, J. Paglione, and R. L. Greene, “Link between spin fluctuations and electron pairing in copper oxide superconductors.,” *Nature* **476**, 73–5 (2011). 6
- [39] P. M. Grant, “High-temperature superconductivity: The great quantum conundrum.,” *Nature* **476**, 37–9 (2011). 6, 7
- [40] E. Koch, in *Correlated Electrons: From Models to Materials*, E. Pavarini, E. Koch, F. Anders, and M. Jarrell, eds., (Forschungszentrum Jülich GmbH, Julich, Germany, 2012), Chap. 7. Exchange mechanisms. 7
- [41] J. Milton, “Superconductors come of age,” *Nature News*. doi:10.1038/news.2010.527, 2010. 7
- [42] M. K. Wu, J. R. Ashburn, C. J. Torng, P. H. Hor, R. L. Meng, L. Gao, Z. J. Huang, Y. Q. Wang, and C. W. Chu, “Superconductivity at 93 K in a new mixed-phase

- Y-Ba-Cu-O compound system at ambient pressure," Phys. Rev. Lett. **58**, 908–910 (1987). 7
- [43] J. M. Tranquada *et al.*, "Antiferromagnetism in $\text{YBa}_2\text{Cu}_3\text{O}_{6+x}$," Phys. Rev. B **38**, 2477–2485 (1988). 8
- [44] L. Liáng, *YBCO Superconductor Research Progress* (Nova Science Publishers, 2008). 8
- [45] D. Greif, T. Uehlinger, G. Jotzu, L. Tarruell, and T. Esslinger, "Short-Range Quantum Magnetism of Ultracold Fermions in an Optical Lattice," Science 1307 (2013). 8, 206
- [46] S. Trotzky, P. Cheinet, S. Fölling, M. Feld, U. Schnorrberger, a. M. Rey, a. Polkovnikov, E. a. Demler, M. D. Lukin, and I. Bloch, "Time-resolved observation and control of superexchange interactions with ultracold atoms in optical lattices.," Science (New York, N.Y.) **319**, 295–9 (2008). 8
- [47] S. Nascimbène, Y.-A. Chen, M. Atala, M. Aidelsburger, S. Trotzky, B. Paredes, and I. Bloch, "Experimental Realization of Plaquette Resonating Valence-Bond States with Ultracold Atoms in Optcal Superlattices," Phys. Rev. Lett. **108**, 205301 (2012). 8
- [48] K. Kim, M.-S. Chang, S. Korenblit, R. Islam, E. Edwards, J. Freericks, G.-D. Lin, L.-M. Duan, and C. Monroe, "Quantum simulation of frustrated Ising spins with trapped ions," Nature **465**, 590–593 (2010). 8
- [49] J. W. Britton, B. C. Sawyer, A. C. Keith, C.-C. J. Wang, J. K. Freericks, H. Uys, M. J. Biercuk, and J. J. Bollinger, "Engineered two-dimensional Ising interactions in a trapped-ion quantum simulator with hundreds of spins," Nature **484**, 489–492 (2012). 8, 9
- [50] J. Simon, W. S. Bakr, R. Ma, M. E. Tai, P. M. Preiss, and M. Greiner, "Quantum simulation of antiferromagnetic spin chains in an optical lattice," Nature **472**, 307–312 (2011). 8

- [51] J. Struck, C. Ölschläger, R. Le Targat, P. Soltan-Panahi, A. Eckardt, M. Lewenstein, P. Windpassinger, and K. Sengstock, “Quantum Simulation of Frustrated Classical Magnetism in Triangular Optical Lattices,” *Science* **333**, 996–999 (2011). 8
- [52] F. Meinert, M. J. Mark, E. Kirilov, K. Lauber, P. Weinmann, A. J. Daley, and H.-C. Nägerl, “Quantum Quench in an Atomic One-Dimensional Ising Chain,” *Phys. Rev. Lett.* **111**, 053003 (2013). 8
- [53] P. Richerme, Z.-X. Gong, A. Lee, C. Senko, J. Smith, M. Foss-Feig, S. Michalakis, A. V. Gorshkov, and C. Monroe, “Non-local propagation of correlations in quantum systems with long-range interactions,” *Nature* **511**, 198–201 (2014). 8
- [54] T. Paiva, Y. L. Loh, M. Randeria, R. T. Scalettar, and N. Trivedi, “Fermions in 3D Optical Lattices: Cooling Protocol to Obtain Antiferromagnetism,” *Physical Review Letters* **107**, 086401 (2011). 9, 101, 200
- [55] S. Fuchs, E. Gull, L. Pollet, E. Burovski, E. Kozik, T. Pruschke, and M. Troyer, “Thermodynamics of the 3D Hubbard Model on Approaching the Néel Transition,” *Physical Review Letters* **106**, 030401 (2011). 9, 52, 101, 195
- [56] D. C. McKay and B. DeMarco, “Cooling in strongly correlated optical lattices: prospects and challenges,” *Reports on Progress in Physics* **74**, 054401 (2011). 9
- [57] J. Imriška, M. Iazzi, L. Wang, E. Gull, D. Greif, T. Uehlinger, G. Jotzu, L. Tarruell, T. Esslinger, and M. Troyer, “Thermodynamics and Magnetic Properties of the Anisotropic 3D Hubbard Model,” *Phys. Rev. Lett.* **112**, 115301 (2014). 9
- [58] T. A. Corcovilos, S. K. Baur, J. M. Hitchcock, E. J. Mueller, and R. G. Hulet, “Detecting antiferromagnetism of atoms in an optical lattice via optical Bragg scattering,” *Phys. Rev. A* **81**, 013415 (2010). 9, 78, 148, 192
- [59] M. Rigol, T. Bryant, and R. R. P. Singh, “Numerical Linked-Cluster Approach to Quantum Lattice Models,” *Phys. Rev. Lett.* **97**, 187202 (2006). 9, 185

- [60] P. M. Duarte, “Band structure calculations for an optical lattice,” <http://dx.doi.org/10.5281/zenodo.11612>, 2014. 11
- [61] O. Morsch and M. Oberthaler, “Dynamics of Bose-Einstein condensates in optical lattices,” Rev. Mod. Phys. **78**, 179–215 (2006). 11
- [62] J. C. Slater, “A Soluble Problem in Energy Bands,” Phys. Rev. **87**, 807–835 (1952). 14
- [63] C. Salomon, G. Shlyapnikov, and L. Cugliandolo, *Many-Body Physics with Ultracold Gases: Lecture Notes of the Les Houches Summer School: Volume 94, July 2010, Lecture Notes of the Les Houches Summer School* (OUP Oxford, 2013). 15
- [64] W. Kohn, “Analytic Properties of Bloch Waves and Wannier Functions,” Physical Review **115**, 809–821 (1959). 15
- [65] F. Schwabl, *Advanced Quantum Mechanics, Advanced texts in physics* (Springer, 2005). 23
- [66] I. Bloch, J. Dalibard, and W. Zwerger, “Many-body physics with ultracold gases,” Rev. Mod. Phys. **80**, 885–964 (2008). 27, 29, 30, 88
- [67] J. Sakurai and J. Napolitano, *Modern Quantum Mechanics* (Pearson Education, 2014), Chap. 6. Scattering theory. 29
- [68] T. Busch, B. Englert, K. Rzazewski, and M. Wilkens, “Two cold atoms in a harmonic trap,” Foundations of Physics pp. 549–559 (1998). 29
- [69] F. Werner, O. Parcollet, A. Georges, and S. R. Hassan, “Interaction-Induced Adiabatic Cooling and Antiferromagnetism of Cold Fermions in Optical Lattices,” Phys. Rev. Lett. **95**, 056401 (2005). 30, 31, 32, 199
- [70] R. Jördens, Ph.D. thesis, ETH Zürich, 2010. 48, 137
- [71] M. Mark, Ph.D. thesis, Innsbruck, 2012. 30

- [72] K. E. Strecker, G. B. Partridge, and R. G. Hulet, “Conversion of an Atomic Fermi Gas to a Long-Lived Molecular Bose Gas,” *Phys. Rev. Lett.* **91**, 080406 (2003). 32, 138, 139
- [73] G. Zürn, T. Lompe, a. N. Wenz, S. Jochim, P. S. Julienne, and J. M. Hutson, “Precise Characterization of ^6Li Feshbach Resonances Using Trap-Sideband-Resolved RF Spectroscopy of Weakly Bound Molecules,” *Physical Review Letters* **110**, 135301 (2013). 32, 139
- [74] W. Heisenberg, “Zur Theorie des Ferromagnetismus,” *Zeitschrift fü Physik* **49**, 619–636 (1928). 33
- [75] J. Hubbard, “Electron Correlations in Narrow Energy Bands,” *Proceedings of the Royal Society of London. Series A. Mathematical and Physical Sciences* **276**, 238–257 (1963). 34, 35
- [76] M. C. Gutzwiller, “Effect of Correlation on the Ferromagnetism of Transition Metals,” *Phys. Rev. Lett.* **10**, 159–162 (1963). 35
- [77] J. Kanamori, “Electron Correlation and Ferromagnetism of Transition Metals,” *Progress of Theoretical Physics* **30**, 275–289 (1963). 35
- [78] R. Scalettar, “QUEST: QUantum Electron Simulation Toolbox,” <http://quest.ucdavis.edu/tutorial/hubbard7.pdf>, 2013. 35
- [79] N. F. Mott, “The Basis of the Electron Theory of Metals, with Special Reference to the Transition Metals,” *Proceedings of the Physical Society. Section A* **62**, 416 (1949). 38
- [80] N. F. Mott, “Metal-Insulator Transition,” *Rev. Mod. Phys.* **40**, 677–683 (1968). 38
- [81] P. M. Duarte, “A few simple treatments of the Hubbard model,” <http://dx.doi.org/10.5281/zenodo.11558>, 2014. 39

- [82] F. Göhmann and S. Murakami, “Algebraic and analytic properties of the one-dimensional Hubbard model,” Journal of Physics A: Mathematical and General **30**, 5269 (1997). 42
- [83] R. Schumman, “Thermodynamics of a 4-site Hubbard model by analytical diagonalization,” . 43, 44
- [84] A. Leggett, *Quantum Liquids: Bose condensation and Cooper pairing in condensed-matter systems*, Oxford Graduate Texts (OUP Oxford, 2006). 43
- [85] C. C. Tsuei, J. R. Kirtley, Z. F. Ren, J. H. Wang, R. H., and Z. Z. Li, “Pure $d_{x^2-y^2}$ order-parameter symmetry in the tetragonal superconductor $Tl_2Ba_2CuO_{6+\delta}$,” Nature **387**, 481–483 (1997). 43
- [86] C. C. Tsuei and J. R. Kirtley, “Pairing symmetry in cuprate superconductors,” Rev. Mod. Phys. **72**, 969–1016 (2000). 43
- [87] D. J. Scalapino and S. A. Trugman, “Local antiferromagnetic correlations and dx^2-y^2 pairing,” Philosophical Magazine Part B **74**, 607–610 (1996). 44
- [88] G. Mahan, *Many-Particle Physics, Physics of Solids and Liquids* (Springer, 2000). 47
- [89] J. Henderson, J. Oitmaa, and M. Ashley, “High-temperature expansion for the single-band Hubbard model,” Physical Review B **46**, 6328–6337 (1992). 47, 48, 185
- [90] M. Rigol, A. Muramatsu, G. G. Batrouni, and R. T. Scalettar, “Local Quantum Criticality in Confined Fermions on Optical Lattices,” Phys. Rev. Lett. **91**, 130403 (2003). 51
- [91] R. W. Helmes, T. A. Costi, and A. Rosch, “Mott Transition of Fermionic Atoms in a Three-Dimensional Optical Trap,” Phys. Rev. Lett. **100**, 056403 (2008). 52
- [92] S. Chiesa, C. N. Varney, M. Rigol, and R. T. Scalettar, “Magnetism and Pairing of Two-Dimensional Trapped Fermions,” Phys. Rev. Lett. **106**, 035301 (2011). 51

- [93] R. Scalettar, “Computational Quantum Magnetism. Lecture III: Determinant Quantum Monte Carlo,” http://boulder.research.yale.edu/Boulder-2003/reading/scalettar_3.pdf, 2003. 52
- [94] R. Blankenbecler, D. J. Scalapino, and R. L. Sugar, “Monte Carlo calculations of coupled boson-fermion systems. I,” Phys. Rev. D **24**, 2278–2286 (1981). 52, 185
- [95] M. Rigol, T. Bryant, and R. R. P. Singh, “Numerical Linked-Cluster Approach to Quantum Lattice Models,” Phys. Rev. Lett. **97**, 187202 (2006). 53
- [96] B. Tang, E. Khatami, and M. Rigol, “A short introduction to numerical linked-cluster expansions,” Computer Physics Communications **184**, 557 – 564 (2013). 53, 185, 222
- [97] S. Chu, “Nobel Lecture: The manipulation of neutral particles,” Rev. Mod. Phys. **70**, 685–706 (1998). 55
- [98] C. N. Cohen-Tannoudji, “Nobel Lecture: Manipulating atoms with photons,” Rev. Mod. Phys. **70**, 707–719 (1998).
- [99] W. D. Phillips, “Nobel Lecture: Laser cooling and trapping of neutral atoms,” Rev. Mod. Phys. **70**, 721–741 (1998). 55
- [100] C. Chin, R. Grimm, P. Julienne, and E. Tiesinga, “Feshbach resonances in ultracold gases,” Rev. Mod. Phys. **82**, 1225–1286 (2010). 55, 137
- [101] M. Houbiers, H. T. C. Stoof, W. I. McAlexander, and R. G. Hulet, “Elastic and inelastic collisions of ^6Li atoms in magnetic and optical traps,” Phys. Rev. A **57**, R1497–R1500 (1998). 56, 132
- [102] P. M. Duarte, Master’s thesis, Rice University, 2011. 59, 65
- [103] G. Ritt, G. Cennini, C. Geckeler, and M. Weitz, “Laser frequency offset locking using a side of filter technique,” Applied Physics B: Lasers and Optics **79**, 363–365 (2004), 10.1007/s00340-004-1559-6. 59

- [104] G. Ferrari, M.-O. Mewes, F. Schreck, and C. Salomon, “High-power multiple-frequency narrow-linewidth laser source based on a semiconductor tapered amplifier,” *Opt. Lett.* **24**, 151–153 (1999). 59
- [105] R. E. Scholten, “Enhanced laser shutter using a hard disk drive rotary voice-coil actuator,” *Rev. Sci. Instrum.* **78**, 026101 (2007). 61
- [106] P. M. Duarte, R. A. Hart, J. M. Hitchcock, T. A. Corcovilos, T.-L. Yang, A. Reed, and R. G. Hulet, “All-optical production of a lithium quantum gas using narrow-line laser cooling,” *Phys. Rev. A* **84**, 061406 (2011). 63, 67
- [107] M. S. Safronova, U. I. Safronova, and C. W. Clark, “Magic wavelengths for optical cooling and trapping of lithium,” *Phys. Rev. A* **86**, 042505 (2012). 72
- [108] M. S. Safronova, B. Arora, and C. W. Clark, “Frequency-dependent polarizabilities of alkali-metal atoms from ultraviolet through infrared spectral regions,” *Phys. Rev. A* **73**, 022505 (2006). 73, 74
- [109] J. Mitroy, M. S. Safronova, and C. W. Clark, “Theory and applications of atomic and ionic polarizabilities,” *Journal of Physics B: Atomic, Molecular and Optical Physics* **43**, 202001 (2010). 73, 74
- [110] T.-L. Yang, Master’s thesis, Rice University, 2014. 78, 172
- [111] J. Liang *et al.*, “1.5% root-mean-square flat-intensity laser beam formed using a binary-amplitude spatial light modulator,” *Applied optics* **48**, 1955–1962 (2009). 83
- [112] A. L. Gaunt, T. F. Schmidutz, I. Gotlibovych, R. P. Smith, and Z. Hadzibabic, “Bose-Einstein Condensation of Atoms in a Uniform Potential,” *Phys. Rev. Lett.* **110**, 200406 (2013). 83
- [113] C. J. M. Mathy, D. a. Huse, and R. G. Hulet, “Enlarging and cooling the Néel state in an optical lattice,” *Physical Review A* **86**, 023606 (2012). 89

- [114] P. N. Ma, K. Y. Yang, L. Pollet, J. V. Porto, M. Troyer, and F. C. Zhang, “Influence of the trap shape on the detection of the superfluid–Mott-insulator transition,” Phys. Rev. A **78**, 023605 (2008). 89
- [115] K. M. O’Hara, M. E. Gehm, S. R. Granade, and J. E. Thomas, “Scaling laws for evaporative cooling in time-dependent optical traps,” Phys. Rev. A **64**, 051403 (2001). 98, 99, 169
- [116] M. Köhl, “Thermometry of fermionic atoms in an optical lattice,” Physical Review A **73**, 031601 (2006). 99, 202
- [117] E. Kozik, E. Burovski, V. W. Scarola, and M. Troyer, “Néel temperature and thermodynamics of the half-filled three-dimensional Hubbard model by diagrammatic determinant Monte Carlo,” Phys. Rev. B **87**, 205102 (2013). 101
- [118] P. M. Duarte, “LDA solutions for the Hubbard model in a compensated optical lattice, ” <http://dx.doi.org/10.5281/zenodo.11761>, 2014. 110
- [119] W. Ketterle, D. S. Durfee, and S. D. M. Kurn, “Making, probing and understanding Bose-Einstein condensates,” in *Bose-Einstein Condensation in Atomic Gases (Proceedings of the International School of Physics “Enrico Fermi,” Course CXL)*, M. Inguscio, S. Stringari, and C. E. Wieman, eds., (IOS Press, 1999). 111
- [120] W. Ketterle and M. W. Zwierlein, “Making, probing and understanding ultracold Fermi Gases,” Rivista del Nuovo Cimento **31**, 247–422 (2008). 111, 129, 136
- [121] C. C. Bradley, C. A. Sackett, and R. G. Hulet, “Bose-Einstein Condensation of Lithium: Observation of Limited Condensate Number,” Phys. Rev. Lett. **78**, 985–989 (1997). 112
- [122] D. Dries, Ph.D. thesis, Rice University, 2010. 112
- [123] C. C. Bradley, Ph.D. thesis, Rice University, 1996. 112, 125
- [124] C. A. Sackett, Ph.D. thesis, Rice University, 1998. 112

- [125] M. Auzinsh, D. Budker, and S. Rochester, *Optically Polarized Atoms: Understanding Light-atom Interactions* (OUP Oxford, 2010). 114, 116, 117
- [126] A. Edmonds, *Angular Momentum in Quantum Mechanics, Investigations in Physics Series* (Princeton University Press, 1996). 120
- [127] D. Budker, D. Kimball, and D. DeMille, *Atomic Physics: An Exploration Through Problems and Solutions* (Oxford University Press, 2004). 121
- [128] G. Reinaudi, T. Lahaye, Z. Wang, and D. Guéry-Odelin, “Strong saturation absorption imaging of dense clouds of ultracold atoms,” *Optics letters* **32**, 3143–3145 (2007). 127
- [129] P. M. Duarte and E. Yang, “Analyze density profiles of ultracold Fermionic gases,” <http://dx.doi.org/10.5281/zenodo.11760>, 2014. 130
- [130] D. A. Butts and D. S. Rokhsar, “Trapped Fermi gases,” *Phys. Rev. A* **55**, 4346–4350 (1997). 130
- [131] V. W. Scarola, L. Pollet, J. Oitmaa, and M. Troyer, “Discerning Incompressible and Compressible Phases of Cold Atoms in Optical Lattices,” *Phys. Rev. Lett.* **102**, 135302 (2009). 137
- [132] R. Jördens *et al.*, “Quantitative Determination of Temperature in the Approach to Magnetic Order of Ultracold Fermions in an Optical Lattice,” *Physical Review Letters* **104**, 180401 (2010). 137
- [133] T. Rom, T. Best, O. Mandel, A. Widera, M. Greiner, T. W. Hänsch, and I. Bloch, “State Selective Production of Molecules in Optical Lattices,” *Phys. Rev. Lett.* **93**, 073002 (2004). 137
- [134] G. Thalhammer, K. Winkler, F. Lang, S. Schmid, R. Grimm, and J. H. Denschlag, “Long-Lived Feshbach Molecules in a Three-Dimensional Optical Lattice,” *Phys. Rev. Lett.* **96**, 050402 (2006). 137

- [135] S. Taie, R. Yamazaki, S. Sugawa, and Y. Takahashi, “An SU (6) Mott insulator of an atomic Fermi gas realized by large-spin Pomeranchuk cooling,” *Nature Physics* **8**, 825–830 (2012). 137
- [136] U. Schneider, Ph.D. thesis, Johannes Gutenberg Univeritat in Mainz, 2010. 137
- [137] T. St ferle, H. Moritz, K. G nter, M. K hl, and T. Esslinger, “Molecules of Fermionic Atoms in an Optical Lattice,” *Phys. Rev. Lett.* **96**, 030401 (2006). 138
- [138] E. L. Hazlett, Y. Zhang, R. W. Stites, and K. M. O’Hara, “Realization of a Resonant Fermi Gas with a Large Effective Range,” *Phys. Rev. Lett.* **108**, 045304 (2012). 138, 139
- [139] G. Thalhammer, K. Winkler, F. Lang, S. Schmid, R. Grimm, and J. H. Denschlag, “Long-Lived Feshbach Molecules in a Three-Dimensional Optical Lattice,” *Physical Review Letters* **96**, 050402 (2006). 139
- [140] G. Birkl, M. Gatzke, I. H. Deutsch, S. L. Rolston, and W. D. Phillips, “Bragg Scattering from Atoms in Optical Lattices,” *Phys. Rev. Lett.* **75**, 2823–2826 (1995). 147, 148
- [141] M. Weidem ller, A. G rlitz, T. W. H nsch, and A. Hemmerich, “Local and global properties of light-bound atomic lattices investigated by Bragg diffraction,” *Phys. Rev. A* **58**, 4647–4661 (1998). 147
- [142] H. Miyake, G. A. Siviloglou, G. Puentes, D. E. Pritchard, W. Ketterle, and D. M. Weld, “Bragg Scattering as a Probe of Atomic Wave Functions and Quantum Phase Transitions in Optical Lattices,” *Phys. Rev. Lett.* **107**, 175302 (2011). 147, 148
- [143] R. A. Hart, P. M. Duarte, T.-L. Yang, X. Liu, T. Paiva, E. Khatami, R. T. Scalettar, N. Trivedi, D. A. Huse, and R. G. Hulet, “Observation of antiferromagnetic correlations in the Hubbard model with ultracold atoms,” . 147, 189

- [144] M. Weidemüller, A. Hemmerich, A. Görlitz, T. Esslinger, and T. W. Hänsch, “Bragg Diffraction in an Atomic Lattice Bound by Light,” *Phys. Rev. Lett.* **75**, 4583–4586 (1995). 148
- [145] F. Cordobes Aguilar, A. F. Ho, and J. Ruostekoski, “Optical Signatures of Antiferromagnetic Ordering of Fermionic Atoms in an Optical Lattice,” *Phys. Rev. X* **4**, 031036 (2014). 148, 151
- [146] C. Cohen-Tannoudji, J. Dupont-Roc, and G. Grynberg, *Atom-Photon Interactions: Basic Processes and Applications, A Wiley-Interscience publication* (Wiley, 1998). 149, 153
- [147] J. Ruostekoski, C. J. Foot, and A. B. Deb, “Light Scattering for Thermometry of Fermionic Atoms in an Optical Lattice,” *Phys. Rev. Lett.* **103**, 170404 (2009). 149
- [148] B. R. Mollow, “Power Spectrum of Light Scattered by Two-Level Systems,” *Phys. Rev.* **188**, 1969–1975 (1969). 153
- [149] R. Loudon, *The Quantum Theory of Light* (OUP Oxford, 2000). 153
- [150] P. Chaikin and T. Lubensky, *Principles of Condensed Matter Physics* (Cambridge University Press, 2000). 163
- [151] L. Luo, B. Clancy, J. Joseph, J. Kinast, A. Turlapov, and J. E. Thomas, “Evaporative cooling of unitary Fermi gas mixtures in optical traps,” *New Journal of Physics* **8**, 213 (2006). 169
- [152] P. M. Duarte, R. A. HArt, T.-L. Yang, X. Liu, T. Paiva, E. Khatami, R. T. Scalettar, N. Trivedi, D. A. Huse, and R. G. Hulet, “Compressibility of a fermionic Mott insulator of ultracold atoms,” . 181
- [153] T. Paiva, R. Scalettar, M. Randeria, and N. Trivedi, “Fermions in 2D Optical Lattices: Temperature and Entropy Scales for Observing Antiferromagnetism and Superfluidity,” *Phys. Rev. Lett.* **104**, 066406 (2010). 185

- [154] R. Staudt, M. Dzierzawa, and A. Muramatsu, “Phase diagram of the three-dimensional Hubbard model at half filling,” *The European Physical Journal B* **17**, 411–415 (2000). 195, 200
- [155] C. J. M. Mathy and D. A. Huse, “Accessing the Néel phase of ultracold fermionic atoms in a simple-cubic optical lattice,” *Phys. Rev. A* **79**, 063412 (2009). 199
- [156] E. Kozik, E. Burovski, V. W. Scarola, and M. Troyer, “Néel temperature and thermodynamics of the half-filled three-dimensional Hubbard model by diagrammatic determinant Monte Carlo,” *Phys. Rev. B* **87**, 205102 (2013). 200
- [157] R. Grimm, M. WeidemÃijller, and Y. B. Ovchinnikov, “Optical Dipole Traps for Neutral Atoms,” in *Optical Dipole Traps for Neutral Atoms*, Vol. 42 of *Advances In Atomic, Molecular, and Optical Physics*, B. Bederson and H. Walther, eds., (Academic Press, 2000), pp. 95 – 170. 207
- [158] J. P. Gordon and A. Ashkin, “Motion of atoms in a radiation trap,” *Physical Review A* **21**, 1606–1617 (1980). 214, 215
- [159] F. Gerbier and Y. Castin, “Heating rates for an atom in a far-detuned optical lattice,” *Physical Review A* **82**, 013615 (2010). 214
- [160] H. Pichler, a. J. Daley, and P. Zoller, “Nonequilibrium dynamics of bosonic atoms in optical lattices: Decoherence of many-body states due to spontaneous emission,” *Physical Review A* **82**, 063605 (2010).
- [161] J.-F. Riou, A. Reinhard, L. a. Zundel, and D. S. Weiss, “Spontaneous-emission-induced transition rates between atomic states in optical lattices,” *Physical Review A* **86**, 033412 (2012). 214